SAND2018-2330R

Rotary Vapor Compression Cycle
Final Report

Sandia National Laboratories
Arthur Kariya
Wayne Staats
Jeff Koplow

Creative Thermal Solutions
Scott Wujek (Currently at Trane)
Stefan Elbel
Pega Hrnjak

Table of Contents

1. Introduction

Few technologies are as prevalent in modern everyday life as space heating and cooling. Space heating and cooling dictates the level of comfort experienced inside a building, and can even have effects on productivity [1]. At an extreme scale, space heating and cooling enables places such as subzero Alaska and scorching hot Arizona to be more widely inhabited. Aside from moderating comfort, space cooling facilitates the proliferation of other technologies: temperature and humidity control is important for semiconductor and pharmaceutical laboratories [2, 3], as well as for the optimal operation of high performance computing centers/data centers [4].

Space heating and cooling, however, comes at an energy cost. In the residential and commercial sectors in the United States, 31% and 22% of total primary energy consumption was attributed to space heating and cooling [5]. Consequently, improvements in the efficiencies of space heating and cooling may lead to a substantial reduction of nationwide energy consumption. Space heating may be accomplished by any method that adds thermal energy to the room air, such as burning hydrocarbon fuel. Space cooling, however, requires the extraction of thermal energy from the room air and consequent release of the energy elsewhere, typically the outside air. The heat must be transferred from the colder to the hotter air, against the normal direction of heat transfer. This requires energy and typically performed by a heat pump. Since heat pumps are the de facto standard for cooling and frequently used in heating as well, they will be the focus of this report. For heat pumps, the aforementioned level of energy consumption is the direct consequence of 1) the heat transfer limitations at the heat exchanger, and the addition of 2) inefficiencies that arise from the method of implementing space heating and cooling technology.

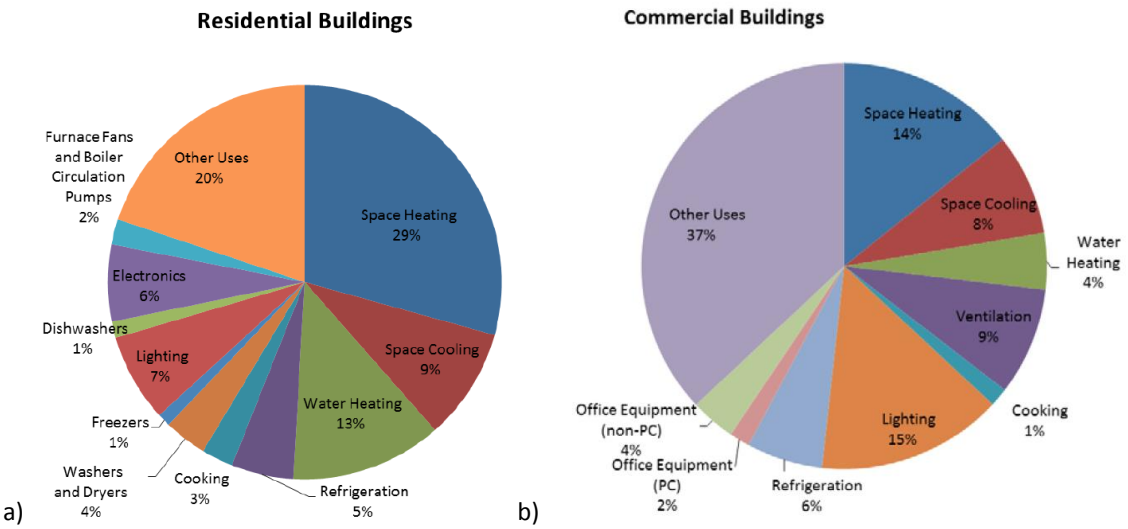

Figure 1. Primary energy usage in US residential (a) and commercial (b) buildings [5].

While there are several heat pump technologies such thermoelectric, adsorption and magnetocaloric cycles, the oldest and most widely used is the vapor compression cycle (VCC). Currently, thermoelectric cycles have not yet achieved efficiencies nor cooling capacities comparable to VCCs. Adsorption cycles offer the benefit of using low-quality heat as the energy input, but are significantly more complex and expensive and are therefore limited to certain niche applications. Magnetocaloric cycles are still in the research phase. Consequently, improvements made for VCCs will likely have the most immediate and encompassing impact. The objective of this work is to develop an alternative VCC topology to reduce the above inefficiencies.

Vapor Compression Cycles

Vapor compression cycles (VCCs) are based on the Joule Thomson cooling of refrigerant fluids, a thermal-mechanical link where the temperature of the fluid decreases as its pressure is isenthalpically decreased. Accordingly, one of the key components of a VCC is the isenthalpic (approximately) expansion valve to decrease the pressure of the refrigerant. The key components consist of the evaporator, condenser, compressor and the expansion valve (Figure 2). The circulation is as follows: high pressure, hot liquid enters the expansion valve (1) and expands to a low temperature and pressure liquid-vapor (two-phase) mixture (2). This mixture enters the evaporator, where the liquid component of the mixture is vaporized by the heat entering the evaporator (3). The fully vapor-phase fluid then enters the compressor, undergoing a pressure increase (4). The high pressure and temperature vapor then enters the condenser, where it condenses to liquid as heat is rejected (1). The temperature-entropy plot for a typical cycle is shown in Figure 3. The VCC therefore can be considered to have two sides – a high pressure and temperature side with the hot condenser heat exchanger interacting with the high temperature air, and a low pressure and temperature side with the cold evaporator interacting with the low temperature air. The two sides are separated by the expansion valve, which decreases the pressure, and the compressor, which increases it.

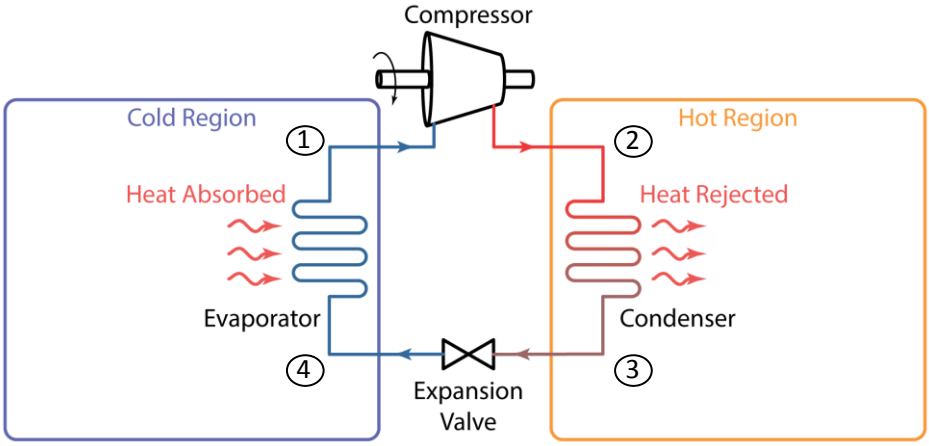

Figure 2. Schematic diagram of a basic VCC system showing the layout of the components.

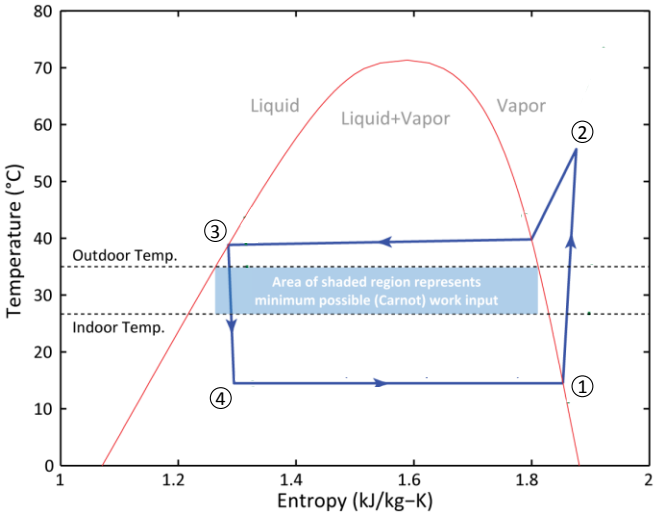

Figure 3. Temperature-entropy diagram of a basic VCC consisting of components shown in Figure 2. The corresponding numbered locations of the cycle are also shown.

Inefficiencies in Vapor Compression Cycles: Heat Transfer

Inefficiencies in VCCs can be traced to the heat exchangers (evaporator and condenser) and the compressor. The evaporator and condenser exchange heat between the air and refrigerant. Several heat transfer coefficients must be considered. At the evaporator, thermal interaction between the evaporator surface (at temperature T_{SURF}) and air (T_{AIR}) is characterized by the air-side heat transfer coefficient (h_{AIR}), and that between the surface (T_S) and refrigerant (T_{REFRIG}) is characterized by the refrigerant-side heat transfer coefficient (h_{REFRIG}). Since the heat gained by the surface from the air is then transferred to the refrigerant, the following equality can be made:

$$Q_L = h_{AIR}A_{AIR}(T_{AIR} - T_S) = -h_{REFRIG}A_{REFRIG}(T_{REFRIG} - T_{SURF}) \quad (1)$$

The expression above assumes that the heat transfer areas on the air-side (A_{AIR}) and the refrigerant side (A_{REFRIG}) may be different. This is the case when fins are used on the air-side. A negative sign is included in the right side expression to indicate that the surface is losing heat to the refrigerant. Using thermal resistance-network analysis, the convective resistance to heat transfer can be defined as:

$$R = \frac{1}{hA} \quad (2)$$

Hence the above equality can be rewritten as:

$$Q_L = \frac{(T_{AIR} - T_S)}{R_{AIR}} = \frac{(T_S - T_{REFRIG})}{R_{REFRIG}} \quad (3)$$

and

$$Q_L = \frac{T_{AIR} - T_{REFRIG}}{R_{AIR} + R_{REFRIG}} = \frac{T_{AIR} - T_{REFRIG}}{R_{HEX}} \quad (4)$$

where R_{HEX} is the total thermal resistance of the heat exchanger. (Note that in deriving the last expression, the conductive resistance across the evaporator body (from the air-side surface to the refrigerant-side surface) was neglected because it is typically 1/100 or 1/1000 of the other two resistances.) Typical values of h_{AIR} are 50-100 W/m^{2}K and h_{REFRIG} are 1000-4000 W/m^{2}K for hydrofluorocarbon refrigerants. Due to the comparatively lower h_{AIR}, area enhancements (fins) are used for the air-side, resulting A_{AIR} being approximately 10-20 times that of A_{REFRIG}.

Common methods of inprovig the air- and refrigerant-side heat transfer include the following:
h_{AIR}: Increasing the air flow rate and/or decreasing the hydraulic diameter (the effective size of the air-flow space) of the flow. While h_{AIR} on the order of 100 W/m^{2}K have been achieved this way, this is limited by the increase in fan power required to draw air through the more restrictive heat exchanger.

A_{AIR}: Adding fin structures to increase the area that interacts with the air. However, compacting more area into a given amount of space results in the same resistance to air flow as described above, and the fins are not isothermal at T_S: hence a temperature drop is incurred in the fins themselves. Despite these limitations, this is a very effective and well-used method of decreasing the thermal resistance; most air-conditioners marketed as high efficiency have noticeably larger heat exchangers (more area) than the standard models. However, this method has limited use for roof-top air-conditioners, where increasing

the size of the heat exchangers can make the air-conditioners prohibitively heavy for safe installation.

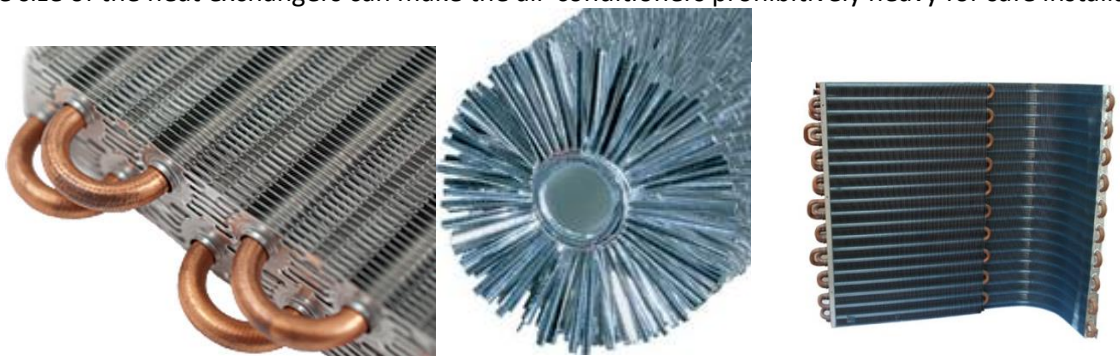

Figure 4. Fins used in heat pump heat exchangers: slit plate fin (left) and spline fin (middle) [6, 7, 8].

h_{REFRIG}: Decreasing the hydraulic diameter of the flow. "Microchannel" versions of VCC heat exchangers (Figure 5) have been produced, with hydraulic diameters on the order of 1 mm (compared to multi-milimeter scale diameters for standard VCC heat exchangers). While microchannel heat exchangers have been in production since the 1990's, only in the past decade have they started to become adopted in the heat pump community. Certain copper tube heat exchangers have gooved inner surfaces to improve refrigerant-surface interaction (Figure 5).

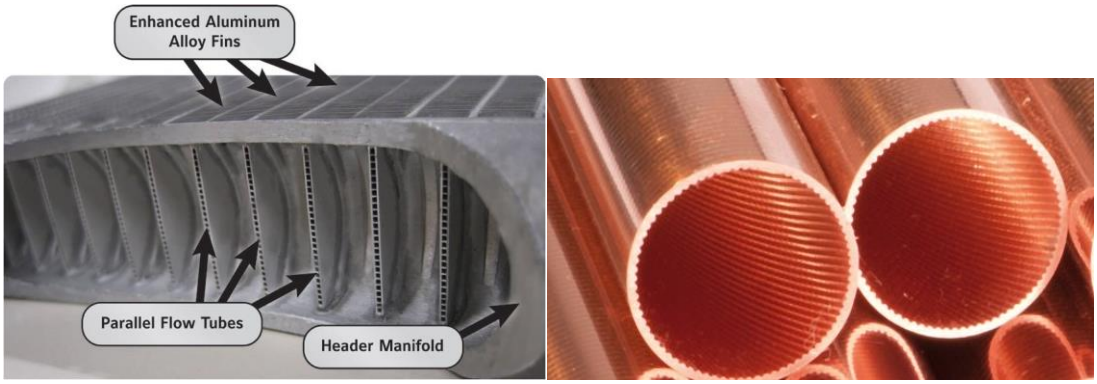

Figure 5. Different types of heat exchanger tubes: microchannel (left) and grooved (right) tube heat exchangers [9, 10].

A_{REFRIG}: Addition of fin-like structures to the internal surface of the refrigerant flow channel/tube. This is infrequently done due to the larger expense to make such channels/tubes.

Inefficiencies in Vapor Compression Cycles: Other Factors

Other inefficiencies can be traced to the compressor and the fouling of the heat exchangers. As compressors in VCCs are designed specifically for vapor, liquid ingestion can be catastrophic; a positive-displacement compressor jammed with liquid will result in broken components (e.g. connecting rod fracture in a piston compressor). To prevent this, the incoming refrigerant (from the evaporator) is superheated to ensure that it is vapor phase. While this is desirable for the longevity of the compressor and VCC, it increases the energy required to compress the refrigerant in the compressor, and is an efficiency penalty. It is also important to note that greater heat transfer inefficiencies in the evaporator and condensers that cause lower evaporator and higher condenser temperatures will directly result in lower evaporator and higher condenser pressures, which will require more energy input to the compressor.

Additional inefficiencies can arise outside of the VCC, on the surfaces of the heat exchangers. Due to the use densely packed fins to increase surface area, the heat exchangers are prone to accumulating dust and debris, which becomes an insulating layer that diminishes heat transfer as well as air-flow. Similarly, it is common for air-conditioner evaporators to collect an insulating layer of condensed water from the cooled air flow. Heat pumps that heat buildings in freezing weather will have frost collecting the evaporator; because the frost does not flow off the evaporator like liquid condensate, a specific "defrost" cycle is required at intermittent periods to recover the thermal performance of the evaporator. The defrost cycle is performed by resistive heating of the evaporator or by operating the VCC in reverse (re-routing the refrigerant flow such that the evaporator and condenser roles are switched).

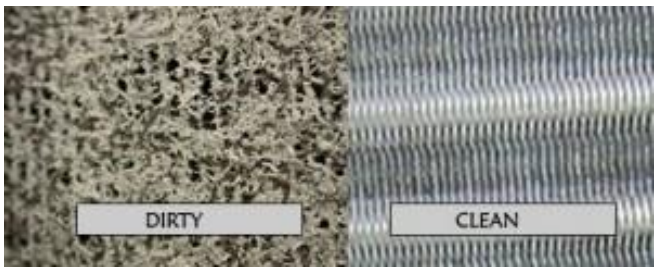

Figure 6. Fouled and clean heat exchanger [11].

Rotary Vapor Compression Cycle

To ameliorate or eliminate these inefficiencies, a new topology was proposed for vapor compression cycles (VCCs). In the baseline RVCC system architecture, the condenser, expansion valve, compressor rotor, and evaporator rotate at high speed on a common shaft as a single modular unit. The rotation of the heat transfer surfaces and the refrigerant generate centrifugal and Coriolis forces, which were predicted to:

1. Improve the air-side convective heat transfer coefficient of both evaporator and condenser. Convective heat transfer in the rotating frame is greatly enhanced by boundary layer thinning, as pioneered in the Sandia Cooler (a TRL 5 heat exchanger technology which is now being adopted by the electronics-cooling industry and is under evaluation for various household applications) [12, 13].
2. Potentially improve the refrigerant-side heat transfer coefficient in both evaporator and condenser. Centrifugal force thins the liquid films in the evaporator and condenser, enabling higher heat transfer coefficients. Additionally, Coriolis force in the evaporator helps stratify the vapor and liquid such to minimize pressure drop in the flow and enhance heat transfer.
3. Eliminate the need for vapor superheating prior to compressor entry. Centrifugal force naturally separates the vapor and liquid phases of the refrigerant in the radial direction, ensuring that only vapor enters the compressor, but without the need for superheating (i.e. centrifugal separation). Elimination of superheating increases vapor density at the compressor intake, resulting in lower compressor input power for a given pressure ratio.
4. Mitigate dust, debris and frost accumulation on the heat exchangers. Rotation of the heat transfer surfaces prevents fouling and the accumulation of frost, as recently shown by researchers at ORNL for a rotating evaporator [14]. Elimination of evaporator frosting results in improved energy efficiency from the elimination of the defrost cycle, in which the evaporator and condenser are temporarily switched to heat the frost.

Figure 7 illustrates the use of an envisioned instantiation of the RVCC as a rooftop A/C and Figure 8

shows a cross section view. As shown in Figure 8, the bulk of the RVCC structure is the condenser and evaporator; they resemble long, multistage axial fans, whose blades contain internal refrigerant flow. The condenser section is the cylindrical core, surrounded by the annular evaporator section. The two sections are separated by thermal insulation, which also has an array of orifices that expand the refrigerant leaving the condenser. The condenser is located at the front of the device, on the center axis of rotation. The VCC itself is not altered; hence all components previously described for the conventional VCC are used in the RVCC as well. The general circulation pathway of the refrigerant is also the same; the refrigerant leaves the compressor as a high pressure and temperature vapor, entering the hollow center axis shaft, which serves as the manifold for entry into the condenser. The vapor flows into radial channels in the condenser, where it condenses, and continues to flow radially outward across the orifice, into the evaporator. Upon entry into the evaporator as a vapor-liquid mixture, the liquid portion is actively centrifuged into the radial evaporator channels, where it is evaporated. The vapor portion, upon entry into the evaporator, directly flows out of the evaporator due to the lack of the centrifuging effect and returns radially inward toward the compressor. The vapor generated in the evaporator channels flows radially inward and joins the main vapor flow exiting the evaporator. While the pressure head generated by the compressor drives bulk flow of the refrigerant, centrifugal force is exploited to assist with liquid and vapor distribution throughout the device; only liquid moves radially outward inside both evaporator and condenser and only vapor is allowed to return radially inward to the compressor.

As a roof-top installation, bidirectional operation as a heater and cooler is achieved by toggling the states of the damper valves on the air-flow ductwork. Thus in the RVCC, bidirectional operation is enabled by switching the flow direction of the air instead of the refrigerant as in conventional bidirectional heat pumps. The entire assembly is rotated by a single variable speed motor and the stator scroll of the compressor is linked via a magnetic coupling to the stationary frame. Alternatively, in a slightly more advanced version of RVCC, the compressor is linked via a magnetic coupling to another variable speed motor operated at a slower speed, where the compressor speed is determined by the relative speed between the two motors (not shown in Figure 7). Note that in the RVCC device architecture, the entire refrigerant loop is hermetic; there are no rotating seals.

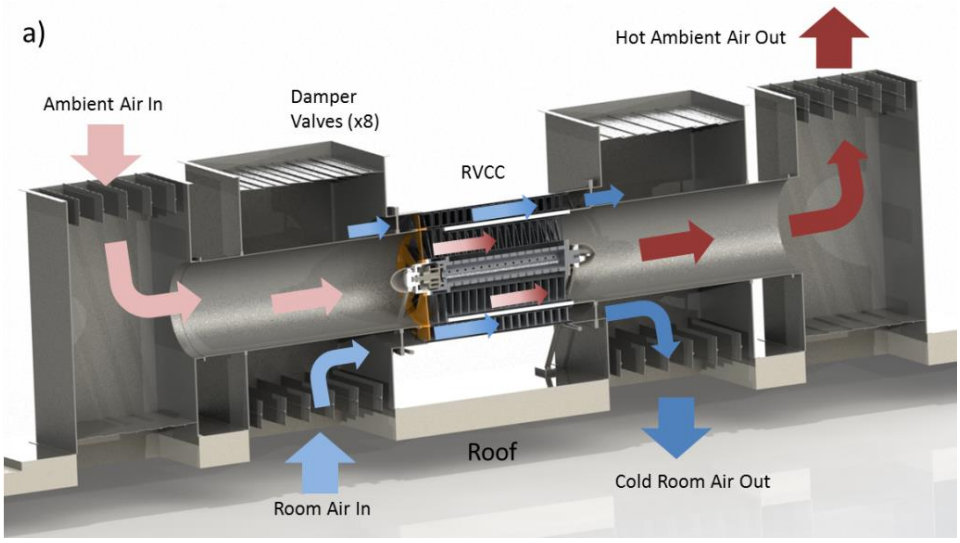

Figure 7. Rooftop installation of the RVCC as a cooler. Damper valves can be toggled to switch operation from cooling to heating mode.

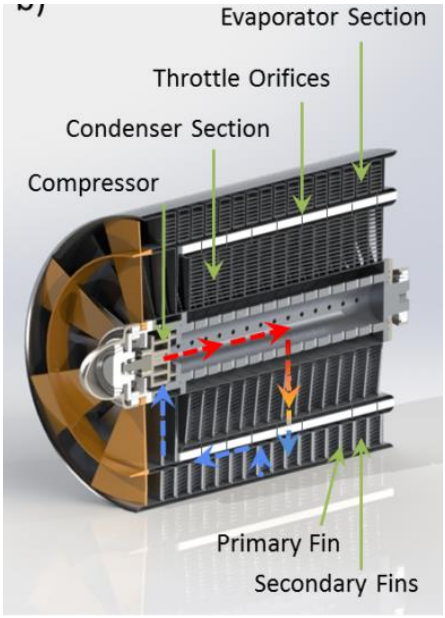

Figure 8. Detailed sectional view of the RVCC showing the components (solid green arrows) and the flow of the refrigerant (dashed lines).

Through the enhancements in heat transfer in both the air- and refrigerant-sides and the elimination of superheating and defrost cycles, the RVCC concept offers potential efficiency improvements over conventional VCCs. However, due to its substantial departure from the conventional implementation of the VCC, several risk-reducing investigations must be performed to assess its technological viability.

2. Scope of Project

This project was the first step in developing the RVCC concept. Accordingly, fundamental risk reduction was emphasized; risks were first prioritized on the basis of how it affected the viability of the concept:

Primary risks

- Operation of VCC in the rotating frame: Can the VCC be made functional in the rotating frame? If no, the basis of the RVCC concept is flawed.
- Unknowns of two-phase flow in the rotating frame: Centrifugal acceleration is predicted to control liquid/vapor distribution such that liquid preferentially moves in the radially outward direction, but this must be confirmed. What determines proper refrigerant charge, and where does excess liquid accumulate when over-filled? Are there any unique two-phase flow characteristics in the rotating frame that were overlooked?
- Enhancement of air-side heat transfer: Is there an enhancement of the air-side heat transfer coefficient in the rotating frame? If there is, what is the magnitude? How effective are fins in the rotating frame? Do fins result in high air-flow pressure drop? The majority of the efficiency improvement relies on enhanced air-side heat transfer.

Secondary Risks

- Liquid film thinning in the condenser via centrifugal acceleration and phase separation in the evaporator channels via Coriolis acceleration: A thinner liquid film in the condenser can improve the condensing heat transfer coefficient by decreasing the conduction distance across the film. Stratification of the liquid and vapor phases in the evaporator through Coriolis acceleration can offer benefits in lower pressure drop and higher heat transfer coefficient. The nature of two-phase flow in the rotating frame is a rather unexplored frontier, however, these benefits are an order-of-magnitude smaller in impact that that from the air-side heat transfer enhancement.
- Lubrication management: Compressor oil, which is integral to the longevity of the compressor, is entrained by the vapor flow leaving the compressor and accommodations must be made to return the oil to the compressor. In the RVCC, oil may collect at the radial end of the device due to centrifugal force. Through literature review, it was found that oil return to the compressor via shear drag by the vapor flow (i.e. a film of oil is dragged back to the compressor by high-velocity vapor flow). As this type of return mechanism can likely be incorporated to the RVCC, the uncertainty associated with this risk was deemed to be secondary.
- Design and integration of a variable orifice expansion valve capable of passive feedback control: Since fixed orifice VCCs are efficient only a single operating point, feedback-controlled variable orifice expansion valves are a necessity for operating efficiently in a range of real world conditions. It is expected that due to the topology of the RVCC, development of such an expansion valve will not simple. However, this was set at a lower priority since, although not ideal, it is still possible to reconfigure the RVCC geometry to incorporate a variable orifice expansion valve that is similar to those in conventional VCCs.
- Manufacturability: Can the RVCC topology be manufactured economically at large volumes? While manufacturability is critical for the future commercial success of the RVCC, this was set at lower priority because commercial production would only be possible if the technology was sound.

This project focuses on understanding and minimizing the primary risks. Work was separated into two parts – 1) understanding the refrigerant-side characteristics and 2) understanding the air-side characteristics and. The logic, scope and intended goals of the two parts are described below.

Understanding Refrigerant-side Characteristics

This portion of the project investigates the general flow phenomena of condensing and evaporating flows and the functionality of a VCC in the rotating frame, specifically focusing on:

1) Theoretically investigating the fundamental operating characteristics of the VCC in rotation, specifically the differences from stationary VCCs.
2) Experimentally testing the RVCC concept in a proof-of-concept prototype, as well as understanding the two-phase fluid flow characteristics in the condenser and evaporator and testing hypotheses from (1) above. The prototype incorporated a full vapor compression cycle with transparent windows in the evaporator and condenser for flow visualization.

Part (1) is covered in Section 3 and part (2) is covered in Section 4. The concepts introduced in Section 3 will be used to describe the trends seen in the data in Section 4. Thermal resistance and saturation pressures were analyzed as a function of the refrigerant flow rate and system rotation speed. Two-phase studies using a complete VCC system in part (2) was critically valuable for observing the dynamics between the evaporator and condenser for different operating conditions.

A note on investigating two-phase flow with computational fluid dynamics (CFD)

At the onset of this project, much deliberation was given to whether part (2) should be performed experimentally or numerically, using CFD. CFD was decided against, as while CFD may initially appear to be an effective method of predicting the flow phenomena, there are several difficulties that arise in its applicability in the present case. CFD models are often based on sub-models that have been previously empirically calibrated. However, because the present study is one of the first investigations into two-phase flow in the rotating frame, prior models do not exist for accurate CFD calculations. This exacerbates the fact that two-phase flow is inherently difficult to predict using CFD. The following are a few reasons for this. Phase change is often bistable; two phases can coexist in steady state but perturbations may be needed to generate one of the phases. The instance of perturbation, as well as the onset of nucleation, is difficult to predict. Furthermore, the existence of a particular phase can drastically change the environment, making a favorable condition for its presence, in effect generating positive feedback. An example of this is a long column of water heated at the base. The hydrostatic head may prevent boiling from occurring, but once boiling is incited, the hydrostatic head is reduced by the presence of vapor, and boiling will continue. As a result, the history of the system may have significant bearing on its current state. Furthermore, grid generation of large scale (>millimeter scale) two-phase interfaces is very computationally intensive. Due to these reasons, highly cited two-phase literature are experimental in nature, such as those of Kandlikar and Thome, often including empirical correlations developed for well-defined experimental conditions.

Understanding Air-side Characteristics

This portion of the project characterizes the air-side heat transfer on

1) a rotating heat transfer body, where the body is a commercially available fan blade, and
2) a rotating array of fins, which are modeled to occupy the space between the neighboring heat transfer blades to enhance the available surface area.

Investigation of (1) was performed experimentally. The transient thermal response of the rotating fan was measured, and subsequently the heat transfer coefficient acting on a rotating body was determined. A rotating infrared thermography system was developed for temperature measurement; synchronous rotation enabled in-situ thermal images. This method was adopted due to the capability of spatial temperature measurement (and hence the calculation of local heat transfer coefficients) while

avoiding intricate wiring into the rotating frame. The experimental data were used to develop a Nusselt number correlation as a function of Reynolds number.

Investigation of (2) was performed with computational fluid dynamics. Representative inter-fin geometries were modeled to determine heat transfer and pressure drop characteristics, which were non-dimensionalized as the J-factor and friction factor. The tradeoff between the heat transfer benefit and the pressure drop penalty in the rotating frame was assessed and compared to the performance of non-rotating air-cooled heat exchangers.

3. Operating Characteristics of the RVCC

While the rotary format of the vapor compression cycle largely shares the same operating characteristics as its stationary, non-rotating counterpart, there are a few notable differences:

1) The system rotation speed can influence the thermal resistance of the system.
2) Excess liquid in the condenser can generate hydrostatic pressure that adds to the total pressure head required at the compressor to pump the refrigerant.
3) Due to the hydrostatic head generated in (2), the RVCC is not a suitable topology for fixed orifice vapor compression systems.

These three points are discussed in detail below. To better understand (3), relevant operating characteristics of a fixed and variable orifice size systems are also described. Thorough understanding of the VCC, and how its operation interfaces with the RVCC, was critical for

Effect of System Rotation Speed

In the RVCC, high centrifugal acceleration enables the use of film condensation and evaporation in the flow channels. This is in contrast to flow condensation and boiling found in the channels in conventional VCC heat exchangers. Figure 9 shows representative flow regimes encountered in flow condensation/boiling. The difference between flow and film-based phase change depends on whether the liquid wetting the surfaces of the channel bridge across the center of the channel to form a slug of liquid. Whether bridging occurs between two surfaces is generally characterized by the Bond number,

$$Bo = \frac{\rho_L a D_h^2}{\sigma_L} \qquad 5$$

where a is acceleration, D_h is the channel hydraulic diameter and ρ_L and σ_L are the liquid density and surface tension, respectively. While the Bond number is not commonly applied to diabatic conditions, its functional dependence on acceleration is nonetheless relevant. As bridging occurs when the Bond number is low (dominated by surface tension), the significantly higher acceleration encountered in rotation allows (874 g at 2000 RPM and 20 cm radius) for even small diameter channels to avoid bridging.

In the case of flow boiling, as the vapor quality (vapor to liquid ratio) increases along the length of the channel, the flow will transition from a bubbly to a more film-like behavior (annular flow, Figure 9) since sufficient liquid is not present to bridge the channel. Since effective escape of the newly formed vapor is a rate-limiting factor during boiling, annular flow typically has the highest heat transfer coefficient during evaporation as it provides a facile escape path at the core of the flow. It is therefore hypothesized that the inherent phase separation between the liquid and vapor afforded by film-based phase-change driven centrifugal acceleration will offer similar benefits in the RVCC.

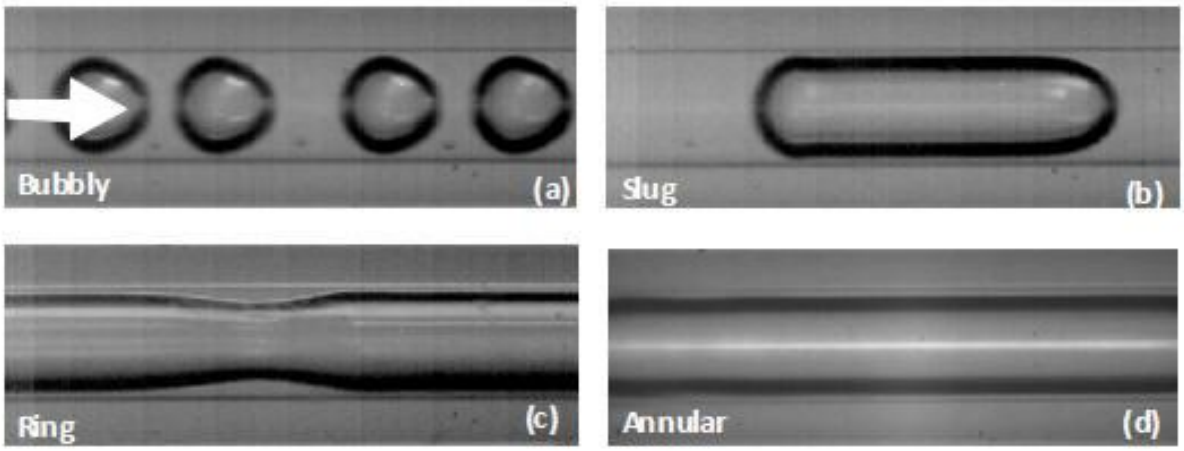

Figure 9. Regimes of flow boiling [15]. Transition from (a) to (d) occur as the vapor quality increases in the flow.

In film condensation, conduction across the liquid film is the rate-limiting step so the thickness of the film is a critical factor in the thermal resistance. The film thickness is a function of the acceleration (Equation 6), where higher acceleration leads to a thinner film [16], where

$$Film\ thickness = \left[\frac{4v_L k_L x(T_{SAT} - T_{SURF})}{h_{fg} a(\rho_L - \rho_V)}\right]^{1/4} \quad 6$$

v_L and k_L refer to the kinematic viscosity and thermal conductivity of the liquid, and x is the distance along the length of the film. Higher rotation speed is therefore expected to reduce the film thickness and thus thermal resistance.

Effect of Excess Liquid in the Condenser

In a rotating condenser, excess liquid will collect at the radial end of the condenser. As shown in Figure 10, this results in a hydrostatic pressure head (ΔP_H) across the pool. Consequently, for a given mass flow and therefore given pressure drop across the expansion device (ΔP_{TH}), the pressure difference between the condenser (P_C) and evaporator (P_E) increases by the amount of the pressure head.

$$P_C - P_E = \Delta P_{TH} + \Delta P_H \quad 7$$

Since the pressure difference between the condenser and evaporator is equivalent to the pressure head required by the compressor, the additional hydrostatic pressure leads to increased compressor load. For a condenser operating at 40 °C and 2000 RPM, the hydrostatic head generated by a 3 cm deep pool at a radius of 20 cm is 3 bar. To put this into perspective, a 3 bar pressure increase at the condenser corresponds to a 1 °C increase in saturation temperature, which is the same result as having higher thermal resistance and is a substantial hit for modern high efficiency condensers.

Excess liquid can be present in the condenser due to 1) over-filling the system with refrigerant and 2) an increase in mass flow rate (heat load) in a fixed orifice vapor compression cycle. How the latter condition affects the liquid volume in the condenser is not as apparent and is elaborated in detail in the following section.

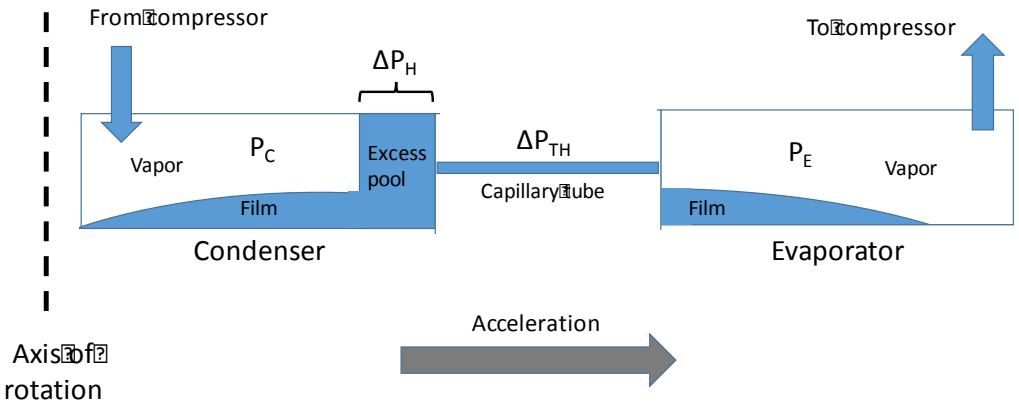

Figure 10. Schematic diagram of condenser and evaporator in rotation, showing locations of liquid. For simplicity, the compressor is omitted and expansion is shown to occur across a capillary tube. P_C, and P_E are the pressures in the condenser and evaporator, respectively, and ΔP_H and ΔP_{TH} are the pressure differences generated by the hydrostatic head and expansion process, respectively.

Effect of Orifice Size Adjustability

While it is becoming common for most 5 ton+ vapor compression systems to use thermostatic expansion valves (TXVs), which allow for mechanical feedback control of the expansion orifice size, many smaller and inexpensive systems, such as window air-conditioners and refrigerators, use fixed orifice expansion through capillary tubes. Fixed orifice systems are tuned for a particular operating point; operating beyond it results in noticeable efficiency degradation. This efficiency degradation is more pronounced in the RVCC topology due to the hydrostatic pressure head in Equation 7.

To maintain generality, only the functional forms of the pressures in Equation 7 will be discussed so that the interplay between the terms can be appreciated. For the purpose of this section, a quantitative modeling effort is inappropriate as exact values are not of concern.

The heat load is linearly related to the mass flow rate ($\dot{m}$) through the latent heat of vaporization (h_{fg}):

$$Q = \dot{m} h_{fg} \tag{8}$$

The pressure drop across the throttling expansion valve is generally characterized to be a quadratic function of the mass flow rate and thus heat load:

$$\Delta P_{TH} = \frac{\dot{m}^2}{C_{TH}^2 A_{TH}^2 \rho_L} \propto Q^2 \tag{9}$$

where C_{TH} and A_{TH} are the orifice coefficient and areas, respectively. In the case of an air-conditioner, the heat load (Q_C, Q_E) must be transferred to the outside ($T_{OUTSIDE}$) and room (T_{ROOM}) air, such that the temperatures of the condenser and evaporator are linearly dependent on the heat load, and thus the mass flow rate.

$$Q_C = \frac{(T_C - T_{OUTSIDE})}{R_{HEX\_C}} \tag{10}$$

$$Q_E = \frac{(T_{ROOM} - T_E)}{R_{HEX\_E}} \quad (11)$$

R_{HEX_C} and R_{HEX_E} refer to the thermal resistances at the condenser and evaporator, respectively. The total energy balance of the system is

$$Q_C = Q_E + W_{COMP} \quad (12)$$

where W_{COMP} is the energy required by the compressor. In this theoretical discussion, "heat load" will refer to both condenser and evaporator heat loads and will only be used for the purpose of referring to their consistent linear relationships to both condenser and evaporator temperatures. This argument is valid when the compressor work input (W_{COMP}) remains constant for any change in heat load considered (through Equation 12), thus maintaining linear proportionality between the condenser and evaporator heat loads. It is also assumed that for the range of heat loads considered, significant changes in thermodynamic properties do not occur and the quality of the two-phase mixture entering the evaporator remains the same.

Equations 10 and 11 reflect snapshots of specific heat exchanger utilizations. Here, utilization refers to the fraction of the condenser and evaporator that is actually used for phase change: regions occupied by liquid in the condenser and vapor in the evaporator decrease utilization. For example, while the entire outer surface area may be used for air-cooling, only a fraction of the condenser surface may be used for vapor condensation as a portion of the condenser may be filled with condensate. Similarly, only a portion of the evaporator may contain liquid and contribute to evaporation/boiling, with the remainder filled with vapor. Utilization therefore is another parameter that affects the heat exchanger thermal resistance via the surface area wetted by the refrigerant for phase change (A_{REFRIG}):

$$R_{HEX} = \frac{1}{h_{AIR}A_{AIR}} + \frac{1}{h_{REFRIG}A_{REFRIG}} \quad (13)$$

As the condenser and evaporator temperatures are both at saturation and linearly proportional to the heat load, the corresponding saturation pressures are also proportional to the heat load. Accordingly, the statements below can be made.

$$Q \propto T_C - T_E \quad (14)$$

$$Q \propto P_C - P_E \quad (15)$$

Figure 11 shows the plots of Equations 9 and 15 on the same graph. Note that the derivation of the linear relationship of Equation 15 from Equation 14 neglects the curvature of the temperature-pressure saturation curve. This, however, does not discount the underlying argument as there is a deterministic relationship between the heat load and $P_C - P_E$. The linearity assumed in Equation 15 is an approximation made to conveniently depict the relationship qualitatively in Figure 11.

The characteristics of the expansion orifice determines the shape of the quadratic curve (solid line), and the thermal resistance of the heat exchangers determines the slope of the $P_C - P_E$ curve (dashed line). If other viscous and inertial pressure drops are neglected (in a properly designed system, they are ~10x smaller) the intersection is the operating point of the VCC, where the pressure difference and mass flow rate are the compressor pumping requirements. This is the point where the pressure difference across

the throttle to drive the appropriate mass flow (corresponding to the heat load) through the orifice equals the pressure difference between the condenser and evaporator that results from the temperatures needed at each heat exchanger to be able to convectively transfer the heat load. By altering the orifice sizing, the steepness quadratic curve can be altered. Figure 12 shows the effect of different orifice sizes; larger sizes have a higher heat load operating point.

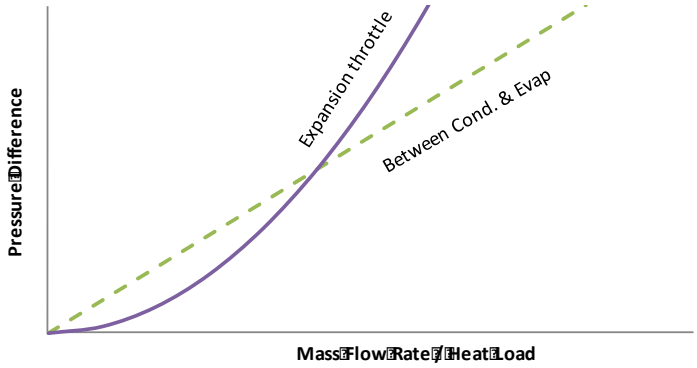

Figure 11. Conceptual graph of the operating point (pressures and heat load) of a simplified VCC.

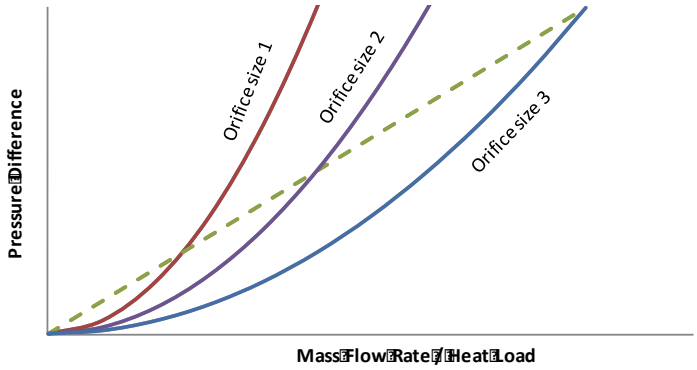

Figure 12. Conceptual graph of VCC operating points for different expansion valve orifice sizes. The plotted curves represent the same pressure differences as in Figure 11.

When the mass flow rate (heat load) is increased via the compressor, the intersection point has to move accommodate the higher heat load. Since the orifice characteristics cannot change, this change is accommodated by the change in heat exchanger utilization. Figure 13 shows this graphically; the slope of the $P_C - P_E$ curve increases. This corresponds to the divergence of the condenser and evaporator temperature, which is accomplished by increasing the thermal resistances at one or both of the heat exchangers by diminishing their utilization. One example of this mechanism is the relocation of liquid from the evaporator to the condenser, thereby decreasing the surface area used for both evaporation and condensation. In this case, the transient that results in the liquid relocation is as follows. As the compressor begins to pump a higher mass flow rate than can be driven across the orifice at the existing $P_C - P_E$, refrigerant accumulates in the condenser. Meanwhile, the compressor is continuously drawing in refrigerant from the evaporator, depleting it. As the utilization of both heat exchanger drops, the condenser pressure rises and evaporator pressure rises until the required $P_C - P_E$ is established such that the mass flow rate at the compressor and orifice are equal.

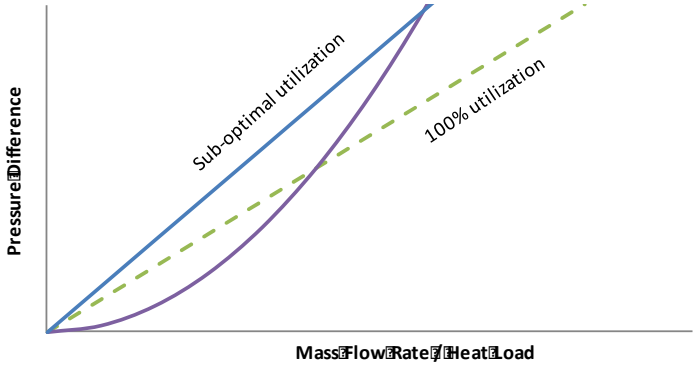

Figure 13. Conceptual graph of VCC operation at a higher heat load than optimal. The plotted curves represent the same pressure differences as in Figure 11.

Figure 10 shows schematically the result lower utilization. Liquid is relocated from the evaporator, where the evaporating film no longer stretches the entire length, to the condenser, where the excess is pooled at the radial end. The area unoccupied by the liquid in the evaporator superheats the vapor. Under high acceleration, the excess liquid results in a non-negligible hydrostatic head, exacerbating the problem of underutilization. Consequently, the RVCC topology is more sensitive to changes in heat load with a fixed orifice, and is a better candidate for operation with a feedback-controlled TXV. TXVs operate by altering the orifice size to accommodate changes in heat load. Similar to that shown in Figure 9, the orifice pressure drop curve adjusts while the $P_C - P_E$ remains unchanged. Specifically, the TXV adjusts the orifice size in order to maintain optimal utilization of the heat exchanger by using the level of evaporator superheat as the feedback control mechanism (high superheat induces an increase in orifice size).

4. Refrigerant-side studies: Experimental Characterization of Rotating VCC and Phase Change Phenomena

A proof-of-concept prototype RVCC was developed to characterize the operation of the VCC and two-phase flow in rotation. Specifically, three main topics were investigated:

1. Characterization of the response of the rotating VCC to heat load changes. This allowed for the confirmation of proper operation using the conceptual framework discussed in Section 4. Through visual access to the condenser and evaporator, the corresponding changes in liquid distribution was recorded.
2. Characterization of the effect of rotation speed. As the rotating VCC was designed to have film condensation and evaporation in the channels, centrifugal acceleration affected the film thickness and thus thermal resistance.

Experimental Apparatus

A custom rotating VCC was developed with visual access to the condenser and evaporator to analyze two-phase flow behavior. Integral components are shown in Figure 14 and consist largely of the rotating VCC assembly with visual access to the condenser and evaporator, rotating camera assembly and the drive motor. During experimentation, the drive motor rotated the rotating VCC assembly while the rotating camera assembly rotated at the same speed (driven by a separate motor) to capture a de-rotated video of the two-phase flow. Details of the individual subassemblies and components are provided in Appendix A.

The condenser and evaporator were fabricated as radial channels in a billet aluminum disc with a polycarbonate lid. Circumferential manifolds connected the channels at the radially inner and outer ends of both condenser and evaporator. To avoid the generation of a hydrostatic head discussed in Section 4, the liquid-collection-manifold at the radial end of the condenser was sized with overcapacity to minimize the hydrostatic height of any excess/transferred liquid. While this was possible in an experimental system, it is not expected to be an appropriate use of space for an actual RVCC device. The refrigerant flow path is shown in Figure 14c, and is similar to that shown in Figure 7. From the centrally located compressor, the refrigerant flows radially outward to the evaporator and returns as vapor radially inward. In the condenser, the vapor condenses in the channels and condensate is drawn radially outward; centrifugal force thus allows for phase separation that can avoid the instabilities and heat transfer inefficiencies of flow condensation. While the flow is uni-directionally radially outbound in the condenser, the evaporator has countercurrent flow: liquid is centrifugally drawn in the radial outbound direction, while the low-density vapor flows radially inward. It was hypothesized that this centrifugally-driven film flow, instead of the more common pressure-driven flow boiling, would provide heat transfer benefits through separation of phases. This flow characteristic is discussed in more detail in the results section. Note that these flow features were incorporated into the design to visually observe the flow characteristics for hypothesis testing, and not for performance optimization.

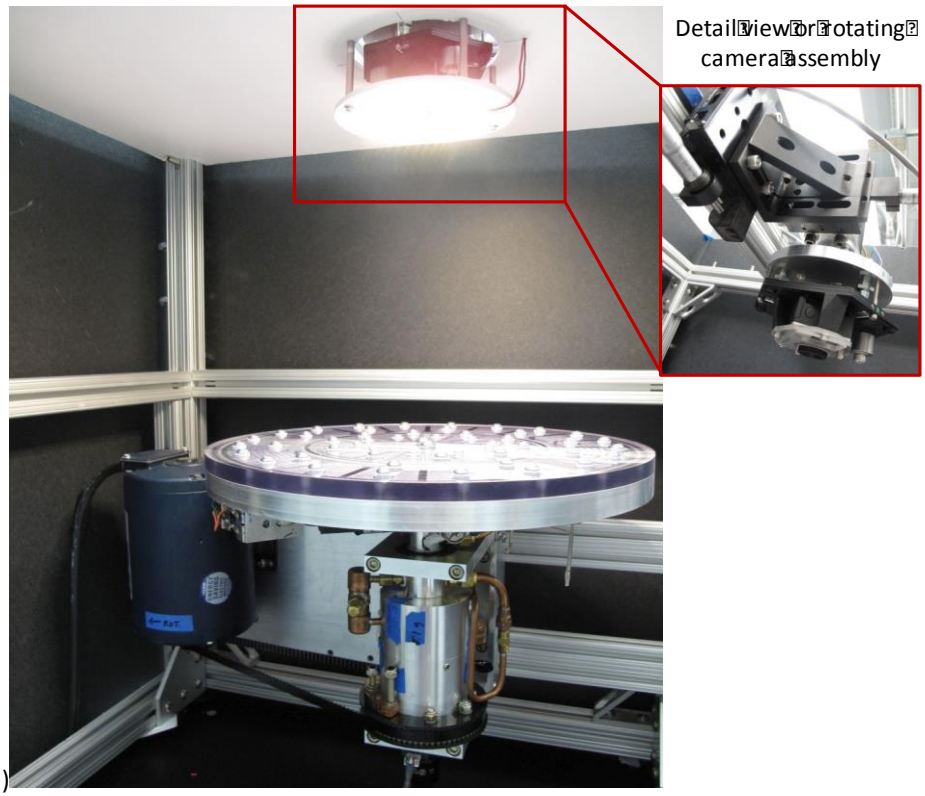
Detail view of rotating camera assembly

a)

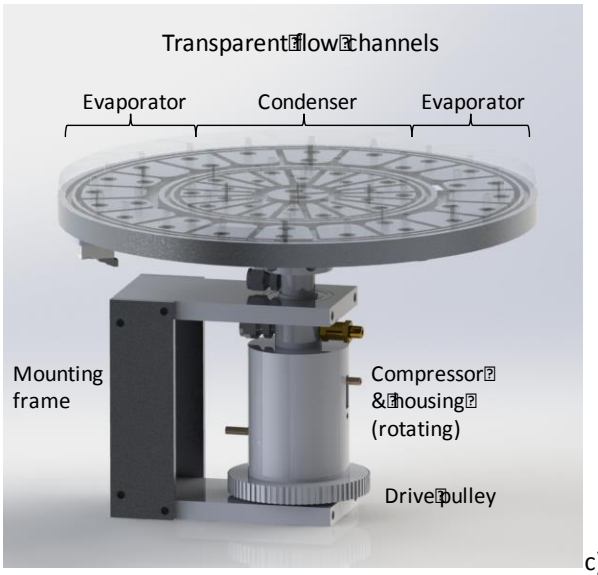
Transparent flow channels
Evaporator
Condenser
Evaporator
Mounting frame
Compressor & housing (rotating)
Drive pulley

b)

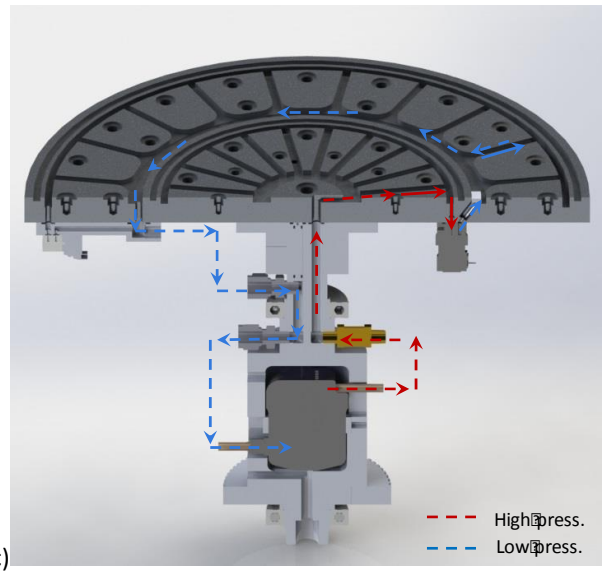
High press.
Low press.

c)

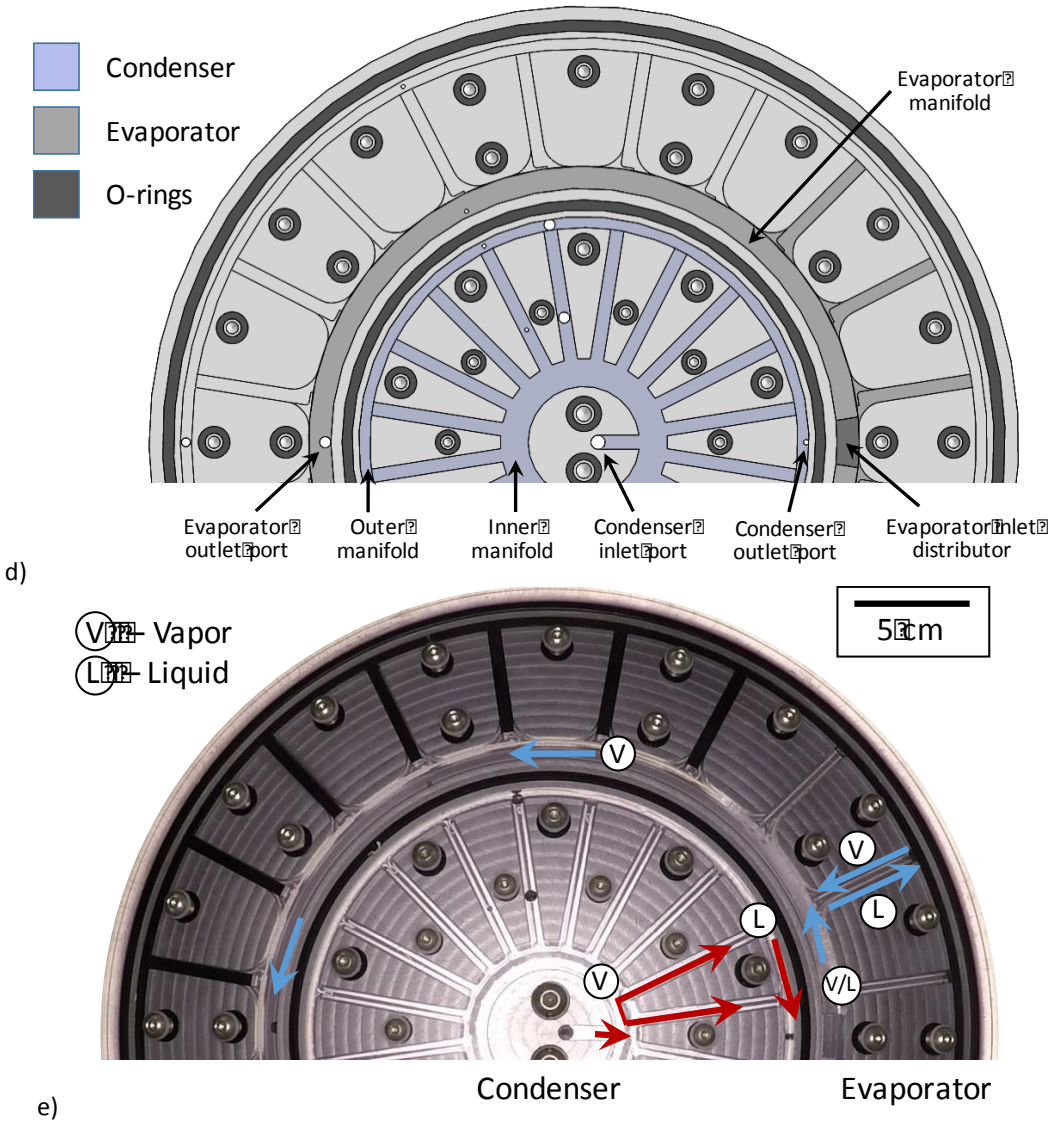

Figure 14. Details of the rotating VCC assembly, showing a) a photograph of the system, b) the individual components, c) refrigerant flow through the system, d) condenser and evaporator sections, and e) flow pattern in the condenser and evaporator.

Experimental Settings

The basic operation of the rotating VCC was characterized at a refrigerant charge of 45 g, compressor speeds ranging from 2450 to 5340 RPM* and system rotational speeds from 50 to 150 RPM. Through preliminary testing, this charge amount was deemed to be ideal; any charging higher resulted in excess liquid in the radial ends of the condenser and evaporator. The expansion valve was kept nearly fully open by energizing the solenoid to 8.4 V, as lower voltages resulted in high condenser pressure that triggered the pressure relief valve. Larger orifice sizes were tested to allow for higher flow rates, but resulted in insufficient expansion. (*approximate compressor speed, calculated from manufacturer specifications)

While the expanded refrigerant was expected to spread azimuthally around the inner evaporator

manifold, it was found that the strong centrifugal acceleration resulted in only partial spreading, as nearly all of the liquid phase immediately entered the channels neighboring the evaporator entrance port. The number of channels with liquid depended on the system RPM, and resulted in relatively incomparable results. However, as the six channels closest to the entrance port were always wetted, the remaining channels were blocked off with a plastic spacer so that analysis can be focused on the wetted channels, allowing the results to be compared with each other (Figure 14c and d). Manifold design to promote equal azimuthal fluid delivery was consequently noted to be a critical part of future development.

Background Thermodynamics of Experimental System

To assist in interpreting the results, it is instructive to briefly describe the energy flow in the experimental VCC. A schematic of the components and the energy flows are shown in Figure 15 below. For simplicity, only three temperatures and pressures are considered, those at saturation of the condenser (T_C, P_C) and evaporator (T_E, P_E), and that of the aluminum disc (T_{AL}). Note that treating the aluminum disk as having a single, uniform temperature is a simplification only for the purpose of explanation. The fundamental heat pump energy balance of Equation 12 holds,

$$Q_{C\_TOTAL} = Q_E + W_{COMP} \tag{16}$$

where here, the heat rejected from the condenser to the ambient, Q_H, corresponds to Q_{C_TOTAL} and the heat input to the evaporator, Q_L, corresponds to Q_E. In this experimental setup, a part of the heat rejected from the condenser is transferred to the evaporator:

$$Q_{C\_TOTAL} = Q_{C1} + Q_{C2} \tag{17}$$

where

$$Q_E = Q_{C2} \tag{18}$$

Through substitution, it can be seen that the amount of heat rejected to the ambient is equal to the amount of energy input required at the compressor,

$$W_{COMP} = Q_{C1} \tag{19}$$

which can also be derived by observing the net energy flow for a control volume surrounding the entire experimental device. Using the manufacturer supplied specifications for the compressor and measured data, the COP for the experimental runs were approximated to be slightly higher than 4; Q_E was four times W_{COMP}. Note that the apparently higher COP was possible due to the high conductivity of the aluminum disc, which maintained a relatively low temperature difference between the condenser and evaporator.

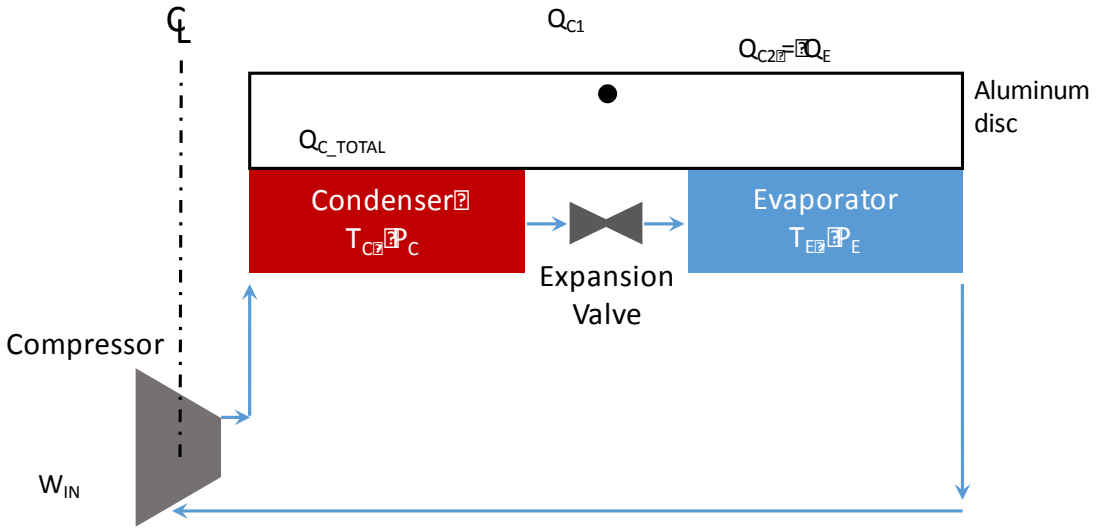

Figure 15. Simplified schematic of rotating VCC experiment showing key temperatures and energy flows.

The discussions on the experimental results refer to three thermal resistances. The condenser thermal resistance occurs between the condensing vapor and the aluminum disk:

$$Condenser\ thermal\ resistance = \frac{T_C - T_{AL}}{Q_{C\_TOTAL}} \quad (20)$$

Similarly, the evaporator thermal resistance occurs between the aluminum disk and the evaporating liquid:

$$Evaporator\ thermal\ resistance = \frac{T_{AL} - T_E}{Q_E} \quad (21)$$

Since the aluminum disk is not actually at a single uniform temperature, where the variation of temperatures is not measured, the above resistances are only referenced at a conceptual level.

Lastly, the "effective thermal resistance" (ETR) is a metric of thermal performance unique to this work, which estimates the total resistances between the condenser and evaporator:

$$Effective\ Thermal\ Resistance = \frac{T_C - T_E}{Q_E} \quad (22)$$

This resistance is due to the condensation and evaporation processes; the resistance of the aluminum disk is negligible. In contrast to the condenser and evaporator resistances above, the ETR is an useful metric in this work because it allows the thermal performance to be quantified with measureable values from the experiments. It is an approximate metric, however, as the amount of heat transferred from the condenser to the ambient, Q_{C1}, (~20 % of total heat leaving the condenser) is not included. Yet, the ETR gives insight to changes in the thermal resistances in the system and is used for that purpose.

Results and Discussion

The rotating VCC was started by first powering all onboard electronics and then initiating system (disk)

rotation. The rotating camera speed was set to match that of the disk and then the compressor was started. With this protocol, the rotating VCC was immediately operational; the startup characteristics are shown in Figure 16 below. Immediately after compressor startup, any liquid content in the evaporator began to boil due to the sudden drop in pressure (a, b), followed by the boiling of the liquid in the expansion valve (c). After this boil-off, there was a delay before a two-phase flow began to enter the evaporator as the expansion valve and entrance region of the evaporator is cooled (d-f). After these regions are cooled, the frothy, two-phase flow began to spread in the evaporator (g). As a greater region of the evaporator in contact with the refrigerant cooled, the two-phase flow spread further around the evaporator (h). Steady state was observed when the region occupied by the two-phase refrigerant was constant. Additionally, through visualization, the ability to centrifugally prevent liquid from returning to the compressor was confirmed: by locating the evaporator exit port in the radially inner most location of the evaporator, no liquid was seen in the port proximity.

In the condenser, while film condensation and centrifugal phase separation is clearly observed, the liquid film is thick at the base of the channels. This is due to the relatively low centrifugal acceleration encountered at the low radial positions in the condenser. As vapor spreads evenly throughout the condenser channels, condensing evenly, axisymmetry in flow is easily achieved. In the evaporator, however, the higher density liquid in the two-phase flow is drawn radially outward by centrifugal acceleration immediately upon entry into the evaporator, and azimuthal spreading is limited. Furthermore, by design, all of the liquid flow in the radial evaporation channels is induced by centrifugal acceleration rather than a compressor-generated pressure gradient. Likewise, due to centrifugal "buoyancy," lower density vapor naturally flows radially inward. This layout was adopted to test an evaporator design that minimizes pressure losses using centrifugal acceleration, where the entire evaporator is at a single pressure (saturation pressure). Additionally, by allowing the newly evaporated vapor to immediately leave the evaporation channels, superheating is minimized. While Figure 16 indicates that these conceptual goals have been achieved, the volume of the radial evaporation channels is not effectively utilized (Figures 16g and h). Considering the opposing flow directions of the vapor and liquid in the radial channels, the channel cross sectional area was designed to be large enough to prevent liquid entrainment by the high-speed vapor leaving the channel. This however, resulted in the liquid occupying a small fraction of the total channel volume. Consequently, while the tested evaporator design has benefits, it is volumetrically inefficient and future evaporator designs will incorporate a more conventional layout, where all the two-phase flow is pressure-driven by the compressor through the evaporation channels, in the radial outbound direction. Feedback control of the expansion valve can be used to maintain low/no superheat.

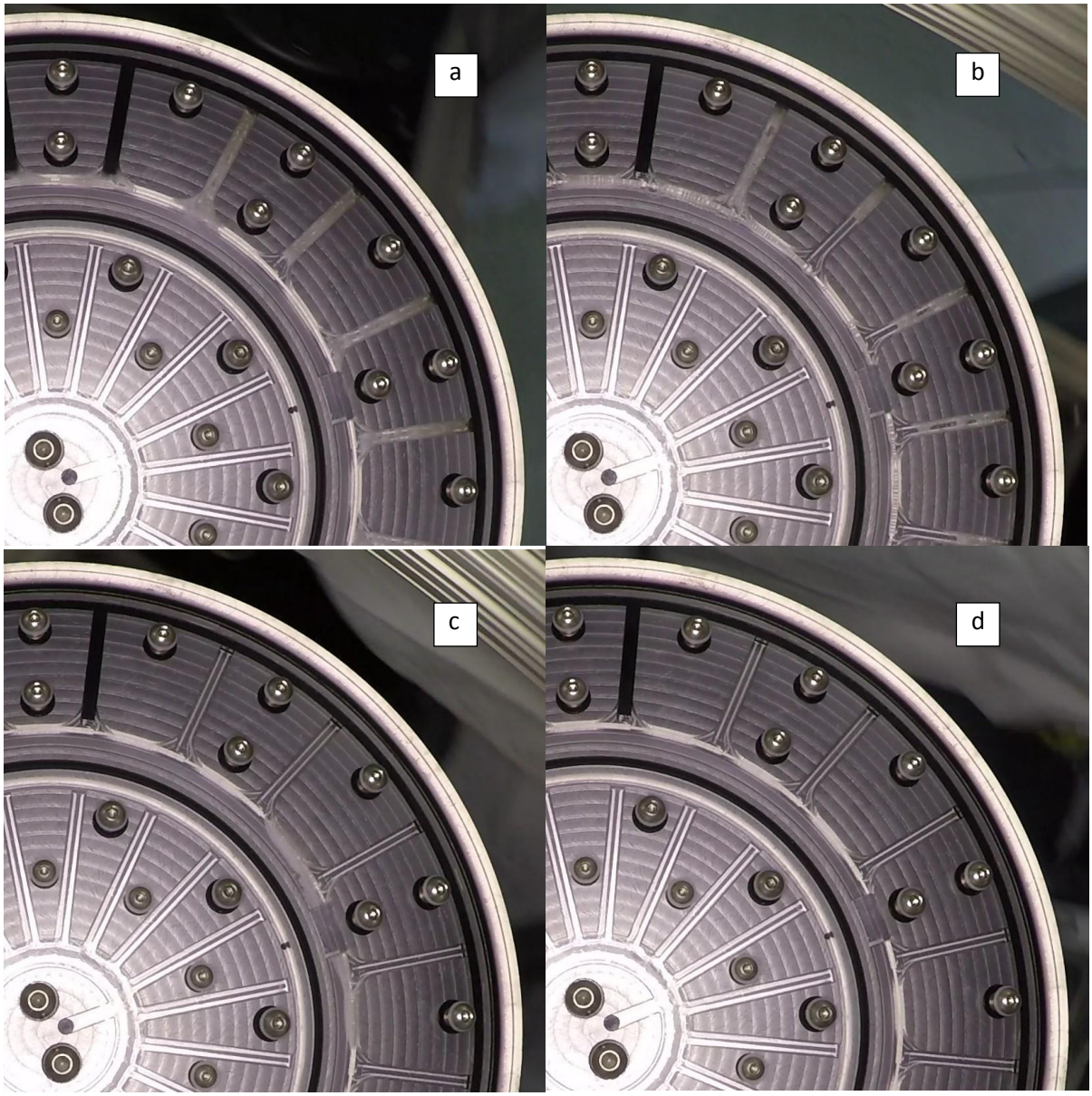
a
b
c
d

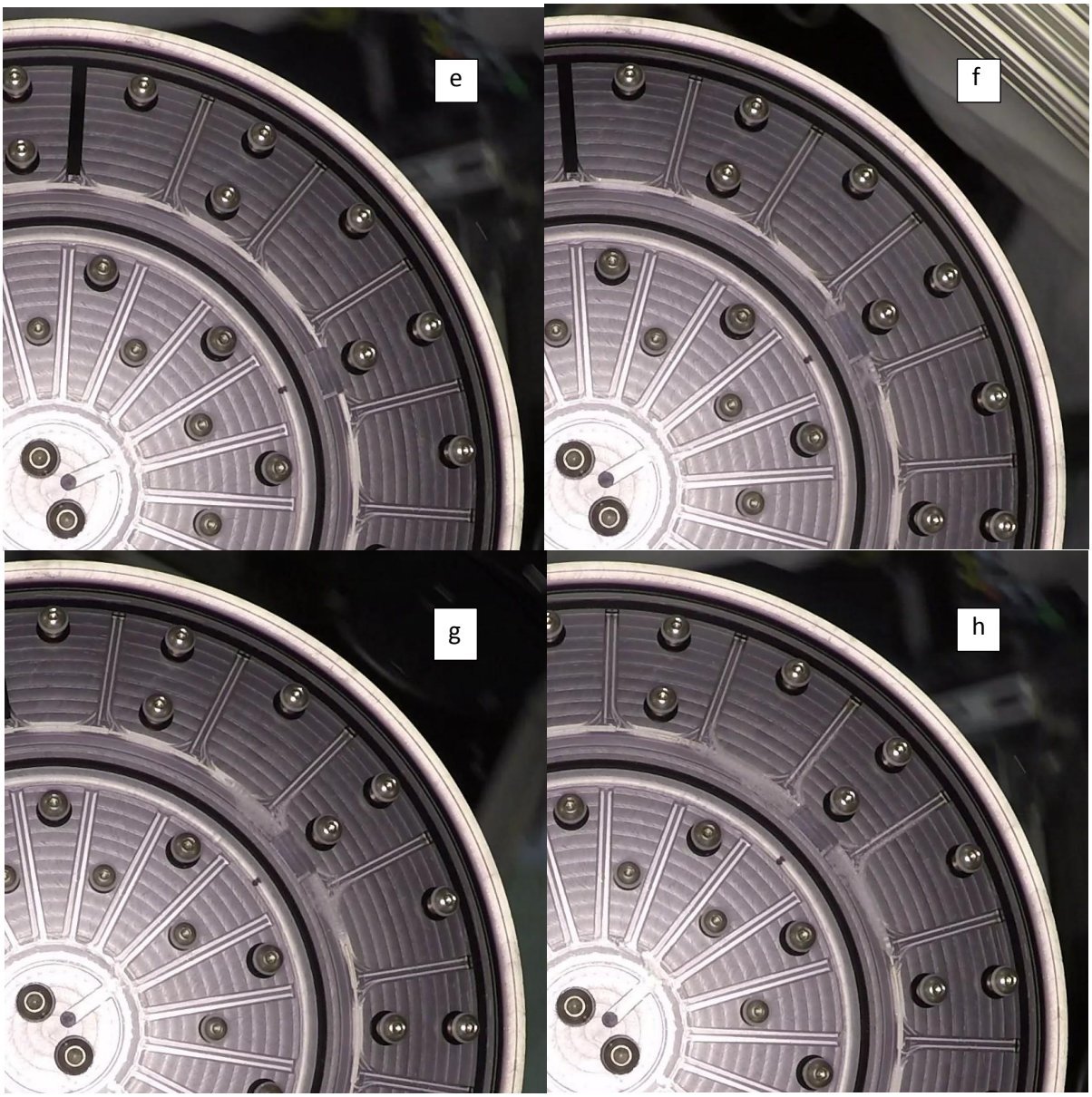

Figure 16. Images taken in succession at startup, at 50 RPM. Images were taken at a) 1 sec. b)6 sec. c) 11 sec. d) 16 sec. e) 21 sec. f) 41 sec. g) 61 sec. h) 80 sec. to show the changes in the fluid flow pattern during startup. The evaporator inlet is most easily seen (via the distribution block and the frothy two-phase flow) in images g) and h).

As the compressor speed (and thus mass flow rate and heat load) was increased, the evaporator pressure fell while the condenser pressure increased (Figure 17). This was expected from Equations 9 and 15, and together with the visual observation of the flashing across the expansion valve, confirmed that the system was functioning properly as a VCC. AS described in Section 4, the greater pressure (and temperature) difference between the condenser and evaporator was afforded by the change in utilizations. Figure 18 shows the relocation of liquid from the evaporator to the condenser that occurs as the compressor speed is increased. The images correspond to the experimental runs shown in Figure 17, and are representative of steady-state operation (i.e. flow conditions were constant, without rapid changes). At higher compressor speed, liquid occupancy of the evaporator noticeably decreases, as seen in the smaller quantity of the frothy mixture and film in the channels. There is a corresponding increase in the liquid volume in the condenser, which can be seen in the change in the vapor-liquid

interface near the radial end of the channels. At low compressor speeds, the outer condenser manifold is only partially filled with liquid, as seen by the sloped phase interface contour in Figure 18a (red circle) and the circumferential interface line in the manifold. When partially filled, the open regions of the manifold, consisting of the aluminum surface and the subcooled refrigerant surface, are available for condensation. At higher compressor speeds, the outer manifold becomes filled, as shown in Figure 18b (red circle). The phase interface occurs where the radial channel meets the manifold, delineating the end of the channel vapor space. Note that even at high compressor speeds, the manifold is not filled with liquid in the area near the condenser exit port due to the exiting flow. This change in utilization is reflected in the change in the ETR, shown in Figure 19: as compressor speed (evaporator heat load) increases, the ETR increases.

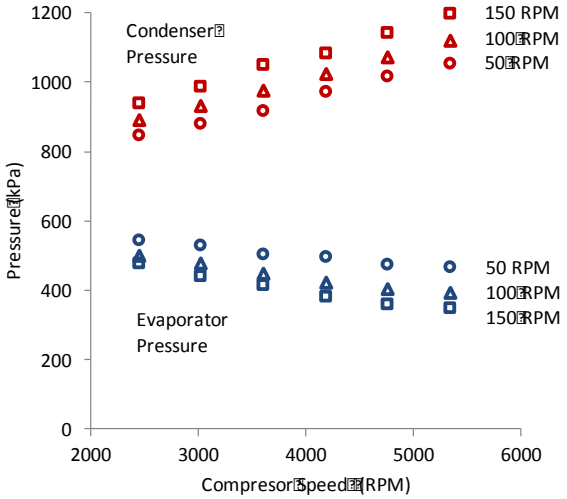

Figure 17. Dependence of condenser and evaporator pressures on compressor speed and disk RPM, with 45 g refrigerant charge.

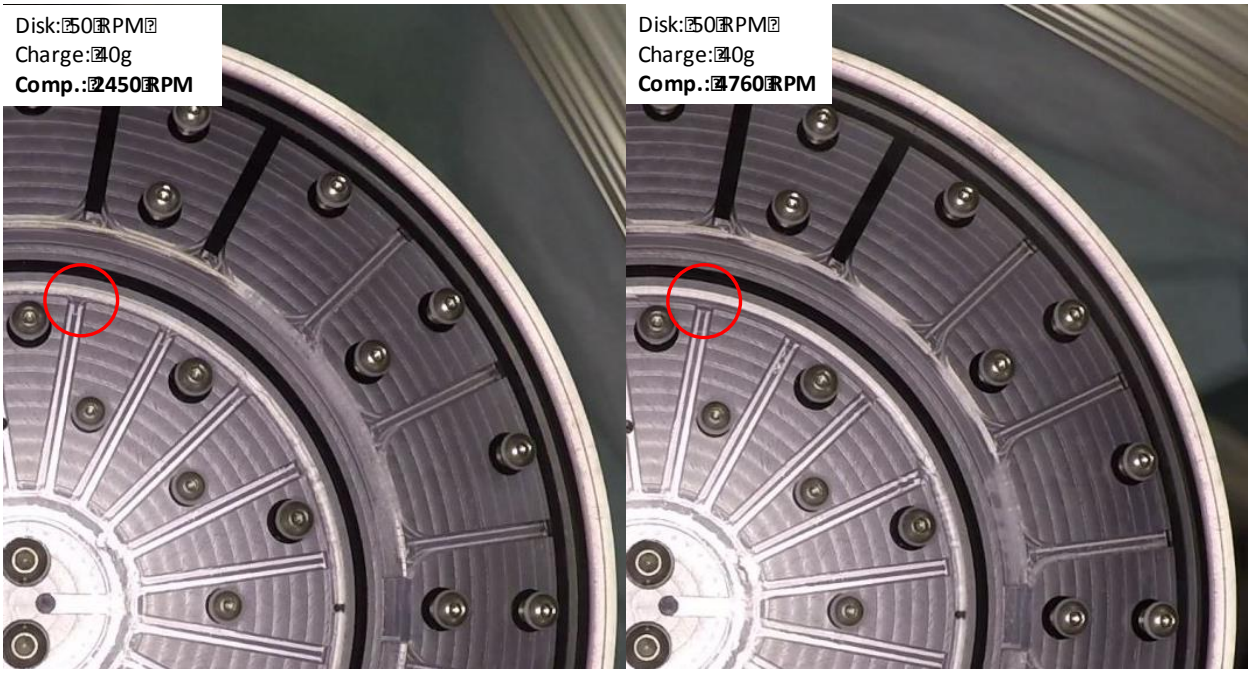

Figure 18. Images of steady state operation at two compressor speeds – a) (left image) at 2450 RPM and b) (right image) at 4760 RPM. Compressor speed represents mass flow rate and thus head load.

Figure 19 shows the ETR as a function of disk speed; ETR decreases with increasing disk speed. The ETR is rather high in general; this is primarily due to the thermal resistance of thick liquid film at the bottom surface of the condenser channels. While this led to higher resistance, it allowed for a more noticeable change in the thermal resistance with disk speed, via centrifugal film thinning. The following subsections discuss the effects of compressor speed, disk speed, and refrigerant charge volume in greater detail.

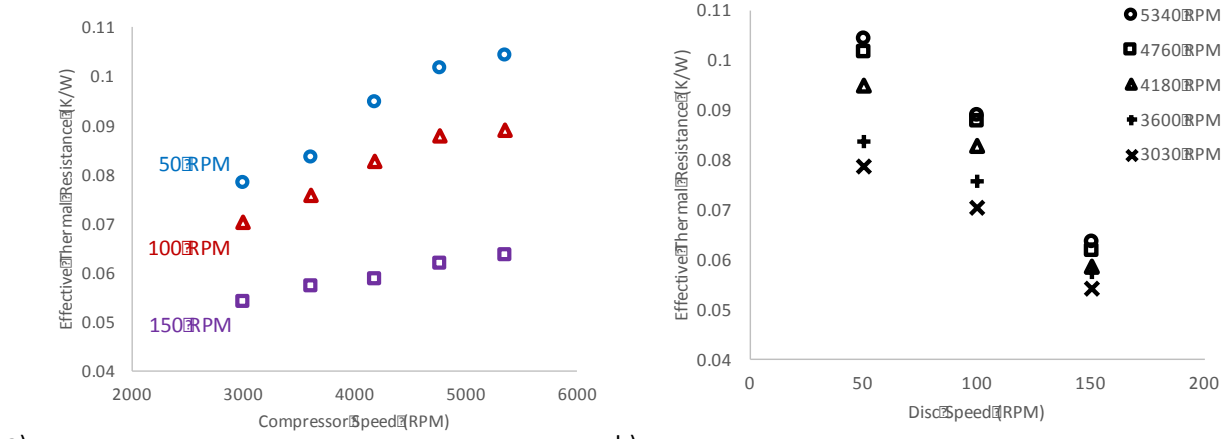

a) b)

Figure 19. Effective thermal resistance, as a function of a) heat load at the evaporator and b) disc speed with a system charge of 45 g R134a.

An increase system rotation speed resulted in a decrease in ETR. As the condenser thermal resistance was dominant in the system due to the thick liquid film, the decrease in ETR is attributed to the decrease in film thickness (Equation 6). The greater acceleration at higher rotation speeds thins the liquid film in the condenser, reducing the conductive thermal resistance across it. While Equation 23 predicts a relative thermal resistance decrease of 47% from 50 to 150 RPM at a compressor speed of 5340 RPM, a 40% decrease was observed. This difference is attributed to the minor change in utilization from the liquid relocation to the condenser.

As the condenser resistance is dominant in the system, the evaporator temperature largely follows the condenser temperature. The evaporator utilization is able to self-adjust so that its (saturation) pressure is below that of the condenser by the amount decreased across the expansion valve (and this in turn determines the temperature difference between the evaporator and condenser). The higher heat transfer afforded by the condenser at a given temperature requires a higher mass flow rate from the compressor, which has a characteristic heat load map as shown below (derived from manufacturer specifications). Since the compressor requires higher evaporator temperatures (and to a lesser degree, lower condenser temperatures) in order to pump the required mass flow rate, the system temperatures adjust accordingly, as shown in Figure 20. Consequently, the greater heat transfer enabled by the lower thermal resistance at higher disk speeds results in the increase in evaporator and condenser temperatures and thus pressures, as seen in Figure 17. This was enabled by the relocation of a small amount of liquid from the evaporator to the condenser, which was visually observed.

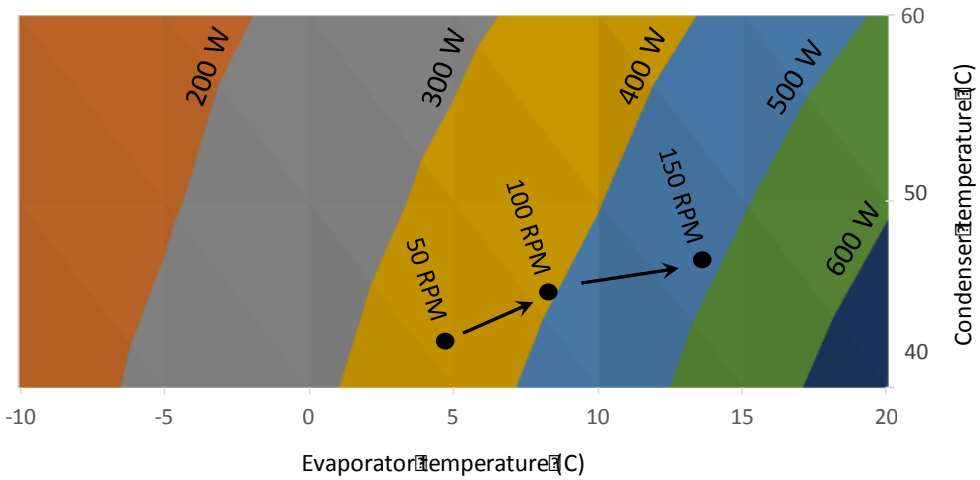

Figure 20. Compressor heat load capacity map, as a function of the evaporator and condenser saturation temperatures. This map was derived from manufacturer specifications, for the case of no superheat nor subcooling. The operating points for the case of 5300 RPM compressor speed with 45 g R134a charge are overlaid to show the changes with disk speed. This particular case is shown because all operating points fell within the map; other cases showed similar trends.

The increase in temperature and pressure with disk speed, despite the improvement in thermal resistance, is a direct consequence of the fixed orifice expansion valve used in these experiments. Higher head loads require larger orifice sizes for less pressure drop across the expansion valve; to better utilize the improvement in the thermal resistance at higher disk speeds, a variable orifice expansion valve, as commonly used in most 2+ ton air-conditioning and refrigeration units, is required. A fixed orifice valve was used in these experiments to minimize experimental complications for clearer analysis.

Summary of Refrigerant-side Investigation

This portion of the investigation addressed the primary risks described in Section 3. First, the functionality of the VCC in the rotating frame was confirmed: the characteristic operation of fixed orifice VCCs was observed in the divergence of the evaporator and condenser pressures with increasing heat load. Second, centrifugal phase separation was confirmed: condensed liquid was drawn to the radial end of the condenser and only vapor was able to return to the compressor in the radial inward direction. Increasing the disk speed enhanced the effect in the condenser, thinning the liquid film and decreasing the thermal resistance. The results, combined with visual observations from the videography, show how the channel space of the evaporator is not effectively utilized; i.e. liquid only occupies a small fraction of the channels. This is due to the inherent design, where the liquid film is drawn into the channels passively by centrifugal acceleration. While the design has benefits in having minimal pressure losses in the flow, the ineffective use of space indicates that in a future iteration, channels with pressure-driven flow that utilize more common flow boiling mechanisms will be a better configuration.

5. Air-side Heat Transfer Study

Measuring the air-side heat transfer coefficient

Due to the importance of air-side convective heat transfer in heat exchangers, many methods for measuring the convective heat transfer coefficient have been developed. Each method has inherent benefits for certain heat exchanger topologies and tradeoffs in terms of accuracy and expense.

Equation 23 shows a generalized version of Equation 1. The convective heat transfer coefficient (h) relates convective heat transfer (Q) and heat flux (q'') to the body's surface area (A) and surface temperature (T_s) and the bulk fluid temperature (T_∞). The heat flux and convective heat transfer coefficient may be defined either locally or as averaged over an area. The convective heat transfer coefficient is generally a function of fluid properties, flow conditions, and surface geometry.

$$Q = q''A = hA(T_s - T_\infty) \qquad 23$$

The form of the above equation guides the methodology used to measure the convective heat transfer coefficient. To determine convective heat transfer coefficients, the other three parameters in the equation must be measured simultaneously: the temperature of the fluid (air), the surface temperature of the solid body, and the heat flux. Methods of heat transfer coefficient measurement can be classified as steady state or transient. Steady state methods allow for a direct determination of the heat transfer coefficient via measurement of the parameters shown in Equation 23, which are steady with time. In contrast, transient methods require the characterization of a temperature response due to a thermal perturbation.

Steady State Methods

Steady state test methods typically utilize a heat source to generate a known amount of heat that is convectively removed, where the temperatures associated with the heat transfer are measured. While electrical heat is generally used because electrical power can be relatively easily measured and controlled, single phase fluids have also been used, where the heat transfer coefficient and temperatures of the fluid flow are well characterized [17, 18]. With a prescribed heat and a known area, the heat flux is readily calculated. Surface temperature measurements can be performed by resistance temperature detectors, thermocouples, or optically. Furthermore, all other surfaces must be well insulated and sufficient time must be given to reach steady state [19].

Another method of determining heat transfer coefficients is to use dedicated thin film heat flux sensors. Such sensors are commercially available and generally consist of a thermopile attached onto both surfaces of a thin sheet of known thickness and material properties. Measurement of the temperature differential across the film allows for the determination of the heat flux across it via Fourier's law. By attaching heat flux sensors to the surface of a body, the convective heat transfer coefficient can be determined with the appropriate temperature measurements. Such sensors are typically accurate to about 10% (Omega Engineering) which is less accurate than the previously described methods. The advantage of such sensors is that they can provide *in situ* measurements with relative ease because they can be adhered to a surface and a few wires can be connected to a precision voltmeter. For this reason, they are used in both engineering and biological applications. However, such sensors modify the heat transfer characteristics of the object to be measured by altering the surface properties and by having a different thermal resistance than the material to which they are applied.

Transient Methods

Many transient methods determine the heat transfer coefficient by characterizing the thermal response due to a thermal perturbation, most often a sudden (step) change in temperature. The thermal response can be most easily understood for a body that is spatially uniform in temperature, something that is very thermally conducting or small in size. Specifically, this spatial uniformity holds when the Biot number (Bi), defined below as a function of the convective heat transfer coefficient (h) and the thermal conductivity (k) and effective length scale (L_C) of the body, is less than 0.1.

$$Bi \equiv \frac{hL_c}{k} \tag{24}$$

(For a thin planar object cooled on both sides, the characteristic length is half the thickness of the material.) For such a body, a sudden change in ambient temperature induces a concomitant change in its temperature. The convective heat transfer rate of Equation 23 is thus directly related to the rate of temperature change (dT/dt) of the body, on the right side of the equation:

$$-hA_s(T - T_\infty) = \rho V c \frac{dT}{dt} \tag{25}$$

via the body's volume (V) density (ρ) and specific heat (c). By knowing the body's initial temperature (T_i) and integrating this equation, the temperature response is found to be an exponential decay:

$$\frac{T - T_\infty}{T_i - T_\infty} = e^{-\left(\frac{hA_s}{\rho V c}\right)t} = e^{-\frac{t}{\tau}} \tag{26}$$

where the thermal time constant (τ) that characterizes the speed of the decay is:

$$\tau = \frac{\rho V c}{hA_s} \tag{27}$$

Equation 26 is useful for experiments, as the thermal time constant, and consequently the heat transfer coefficient, can be determined from the measured temperature decay. This enables heat transfer characterization through a simple experimental framework, but is limited to average heat transfer coefficient analysis for bodies that meet the Biot number criteria described above.

In another method of transient heat transfer characterization, a film of thermochromatic liquid crystals can also be applied to the surface of interest to measure the surface temperature via color change. From a state of thermal equilibrium with the surrounding air, a step change in air temperatures would be applied, and the heat transfer is calculated from the surface temperature by understanding the combined effects of convection, conduction, and sensible heat. The liquid crystals display a dramatic change in color during the temperature change, which can be recorded by photographs or video. This method has the advantages of allowing local heat transfer coefficients to be determined with moderate independence of the properties of the underlying body, requires no physical connections (i.e. no wiring) to the surface of interest, and the ability to achieve good temporal resolution with typical cameras. The main challenges of this technique come from the application of thermochromatic liquid crystals to the surface of the object of interest.

Lastly another method relies on the parallelism between heat and mass transfer due to their similarity in underlying mechanisms. A manifestation of this is the near equivalence in the expressions for the

convective non-dimensional heat and mass transfer numbers, the Nusselt number (Nu) and Sherwood number (Sh), respectively, where the only difference is in the former's dependence on the Prandtl number (Pr) and the latter on the Schmidt number (Sc) [16, 20]. When the Prandtl number equals the Schmidt number, the Nusselt number will equal the Sherwood number. It is instructive to note that both Prandtl and Schmidt numbers are material properties; consequently, Nusselt number can be calculated directly from Sherwood number and vice versa. Therefore, if the mass transfer rate of a substance into an air stream can be measured, then the heat transfer coefficient from the same surface can be calculated. This can be exploited by fabricating the surface/body of interest in a substance like naphthalene (e.g. the traditional chemical used in moth balls), or by depositing a quantity of naphthalene on a heat transfer body. As the substance vaporizes into the air-flow, the amount/rate of mass transfer can be determined by measuring the change in weight. Alternatively, the mass transfer rate can also be determined from the amount of naphthalene in the downstream air. Such a technique has been used by Sparrow and Chastain [21] and by Kearney [22] to measure local heat transfer of finned heat exchangers. While this technique can provide high quality results, including local heat transfer, it is expensive in terms of experimental setup and subsequent analysis.

Measurement of air side heat transfer coefficient in the rotating frame

While the above methods for determining the heat transfer coefficient are useful for systems in the stationary frame, difficulties arise when implementing them in the rotating frame, which is the focus of this work. The act of rotation hinders the use of electronics on the heat transfer body or surface because slip rings or wireless measurement equipment are required. Both can become challenging when the local heat transfer is of interest, as channel counts grow proportionally with the number of regions of interest. Likewise, several optical methods have been employed, but many of these are ill suited for high speed rotation or when the driving temperature differences are relatively small due to associated requirements in temperature resolution. Finally, many of these experiments are very expensive in terms of time and labor to prepare and many of these costs are recurring costs, incurred each time a new geometry is employed. Heaters and measurement devices need to be reinstalled and recalibrated. Despite these difficulties, however, heat transfer research was done as part of NASA's Hot Section Technology program in the late 1980s to study jet turbine engines. Blair and Anderson attached an electrically heated skin to a rigid foam castings of turbine airfoils [23]. The surface temperature was measured with a combination of thermocouples and sprayed thermochromatic liquid crystals. The liquid crystals, which changed color at known temperatures, were monitored with an SLR camera with high speed color film. With this method, care was required in gluing a wrinkle-free metal foil to the foam, and the temperature transition pattern in the liquid crystals was also not discernable when using a roughened surface.

Freund presented a novel approach to measuring heat transfer coefficients with infrared thermography by generating a periodic heat flux with a laser or halogen light [24]. This method relied on measuring the phase lag between temperature and heat flux, and was employed on a wide range of applications and had close agreement with absorption and liquid crystal based methods. As the heat transfer measurement was did not require any alteration to the heat transfer body and surface, substantial flexibility was afforded by this method. However, significant post-processing was necessary. Due to these inherent difficulties in experimentally determining the heat transfer coefficient in the rotating frame, together with the rarity of needing such information, very few studies have addressed this topic.

Non-intrusive thermal characterization with infrared thermography

In developing a method of characterizing the heat transfer coefficient for a body representative of the

RVCC, experimental constraints were first established:

1) The experimental system should allow for facile characterization of different bodies with minimal preparation.
2) In order to achieve 1) above, as well as to minimize hardware complexity and cost, the method should be non-intrusive. That is, the heat transfer body will not be modified or custom-fabricated for the specific purpose of heat transfer measurement. This allows for commercially-available, off-the-shelf bodies to be used when appropriate.

As a result, steady state measurement, which requires a constant addition of heat, was not an option. Similarly, the addition of heat during experimentation, such as with a laser or heat lamp, was avoided due to post-processing difficulty. Optical measurement of surface temperature via films, as well as mass transfer methods, were not an option due to the necessity to modify or custom-fabricate the heat transfer body. Consequently, infrared thermography was chosen for temperature measurement, and a transient technique was adopted where measurement began with a step change in air temperature (hence no active heating during the measurement duration).

As this method measures the transient temperatures of the body surface, several additional considerations are necessary. While Equation 26 can be used to determine *average* heat transfer coefficients for bodies where the Biot number is small, local heat transfer coefficients cannot be determined due to the facility of thermal spreading within the body. It is therefore necessary to establish a theoretical framework, analogous to Equation 26, to allow the heat transfer coefficient to be calculated from the measured local surface temperatures.

Analysis from Schneider [25], as referenced in Incropera and Dewitt [20], expresses the temperature distribution across a plate with air-flow on both sides with Equation 26 below

$$\frac{T - T_\infty}{T_o - T_\infty} = \sum_{n=1}^{\infty} C_n e^{-\zeta_n^2 Fo} \cos\left(\zeta_n \frac{x}{L_{half}}\right) \quad 28$$

Where T_o and T_∞ are the initial and air temperatures, L_{half} is half of the plate thickness and the constants C_n are functions of ζ,

$$C_n = \frac{4 \sin \zeta_n}{2\zeta_n + \sin(2\zeta_n)} \quad 29$$

where ζ are the eigenvalues of the transcendental equation

$$\zeta_n tan\zeta_n = Bi \quad 30$$

The Fourier number, Fo, quantifies the extent of thermal penetration into a body via conduction, defined as:

$$Fo \equiv \frac{\alpha t}{L_{half}^2} \quad 31$$

At Fourier numbers greater than 0.2, sufficient time has passed for thermal penetration to occur, such that the thermal gradient in the direction of heat transfer (i.e. perpendicular to the plate) in the body

becomes negligible. Thus at these Fourier numbers, Equation 28 can be approximated by the first term of the series:

$$\frac{T - T_\infty}{T_o - T_\infty} = \frac{4 \sin \zeta_1 \cos\left(\zeta_1 \frac{x}{L_{half}}\right)}{2\zeta_1 + \sin(2\zeta_1)} e^{-\frac{\zeta_1^2 \alpha t}{L_{half}^2}} \quad 32$$

Note that the functional dependence on time is the same as Equation 26, as expected for thermal decay. In this case, the characteristic thermal time constant is:

$$\tau = \frac{L_{half}^2}{\alpha \zeta_1^2} \quad 33$$

Compared to Equation 26, the time constant is no longer linearly dependent on the convective heat transfer coefficient. However, since ζ_1 must be positive, there is a one-to-one correspondence of the thermal time constant to the heat transfer coefficient, allowing the coefficient to be calculated from Equations 30, 32 and 33. To better understand the potential limits of this method of analysis, Figure 21 shows the relationship between $\zeta_1$and the Biot number for a plate and cylinder [20]. It can be seen that for Biot numbers greater than 5, the dependence on ζ_1 is significantly more sensitive – a small change in ζ_1 causes a substantial change in Biot number. As ζ_1 is the experimentally determined quantity in this work, from which the Biot number is calculated, this increased sensitivity amplifies any experimental uncertainty reflected in ζ_1. Consequently, for this work, the application of this method was limited so that the Biot number did not substantially exceed 5. Despite this limitation, it is noted that this transient thermal characterization method enables a multitude of geometries and materials that do not fit the more stringent Biot number requirement of using Equation 27.

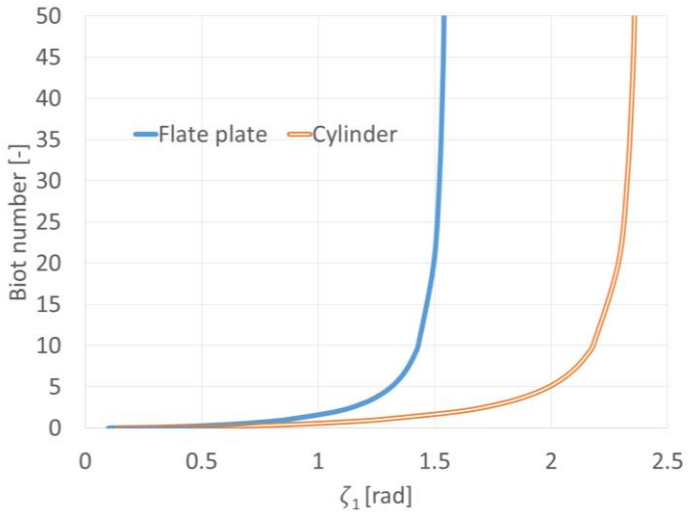

Figure 21. Functional relationship between eigenvalue appearing in thermal time constant and Biot number

Experimental Apparatus

Figure 22 shows the experimental layout for measuring local heat transfer coefficients using the method described above. The rotating heat transfer body was placed in a custom fabricated duct (cross section of 0.75 m x 075 m and length of 2.5 m). The duct was placed inside a temperature-controlled environmental chamber. Flow through the duct was generated/assisted by a secondary fan at the exit of the duct. Thermocouples were installed at the entrance of the duct to measure the temperature of

the entering air flow. Transient temperature response was induced with a 15 kW salamander heater, located 2 m from the duct entrance to ensure uniform temperature at the heat transfer body. After heating the heat transfer body, the heater was shut off, allowing room temperature air to enter the duct and cool the body. Characterization of the temperature decay was initiated when the heater was shut off.

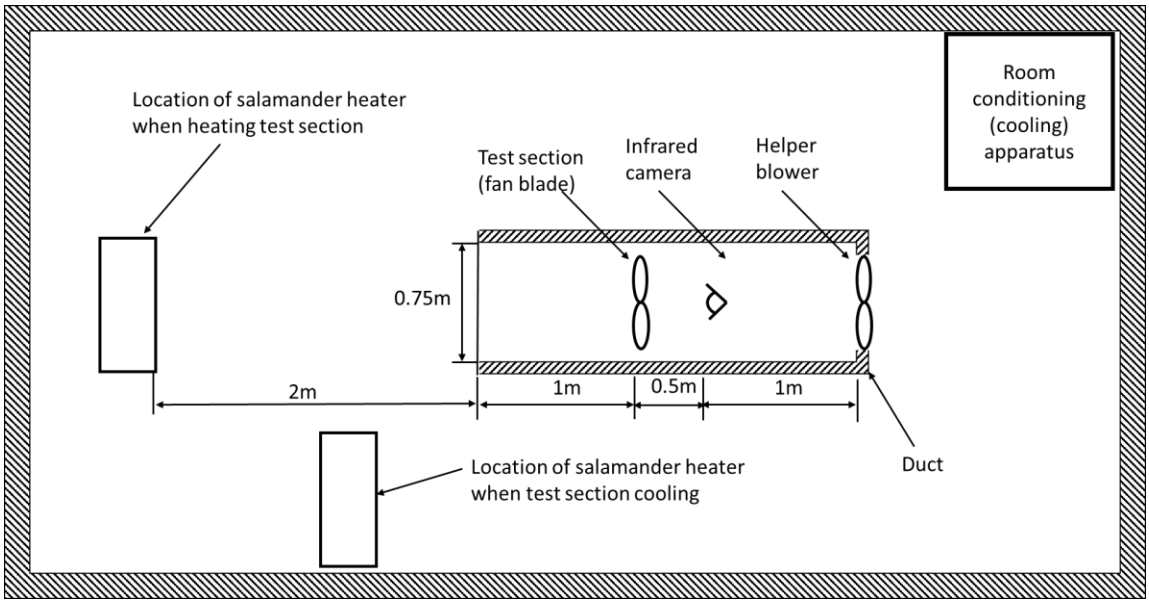

Figure 22. Schematic of experimental layout. Air flows through the test section from left to right.

Figure 23a shows the details inside the duct. The heat transfer body, shown as a three-blade plastic fan, is rotated by a motor-driven pulley. The motor drive shaft also rotates second pulley, which spins an infrared image acquisition system. Using the same motor and pulley ratios to drive both heat transfer body and camera ensures synchronous rotation for de-rotated videography. Figure 23b shows the details of the rotating infrared image acquisition system, which consists of a FLIR Quark infrared camera, a microprocessor controller for the camera (Raspberry Pi 2) and a battery pack.

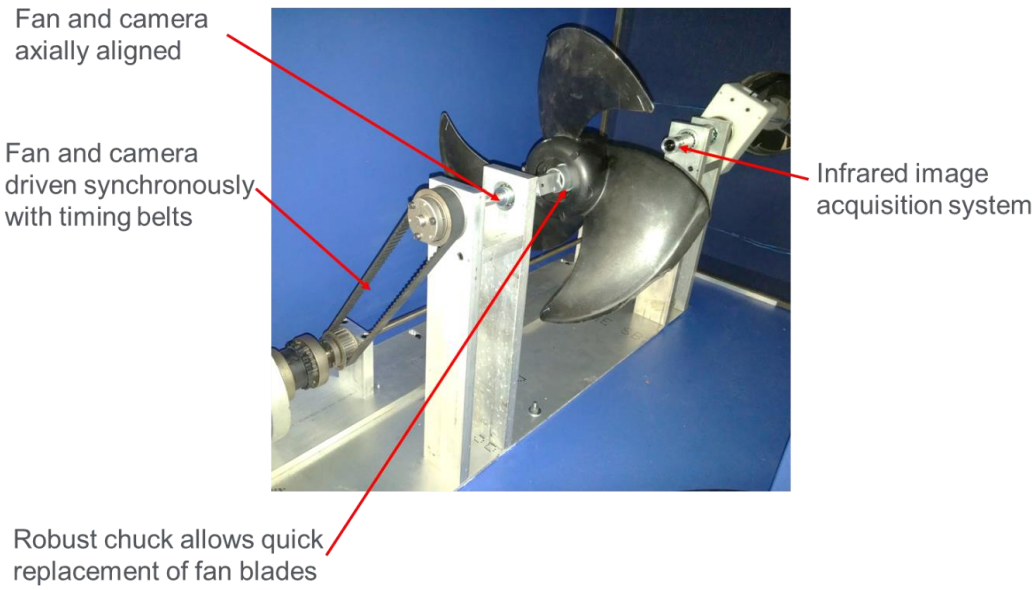

a)

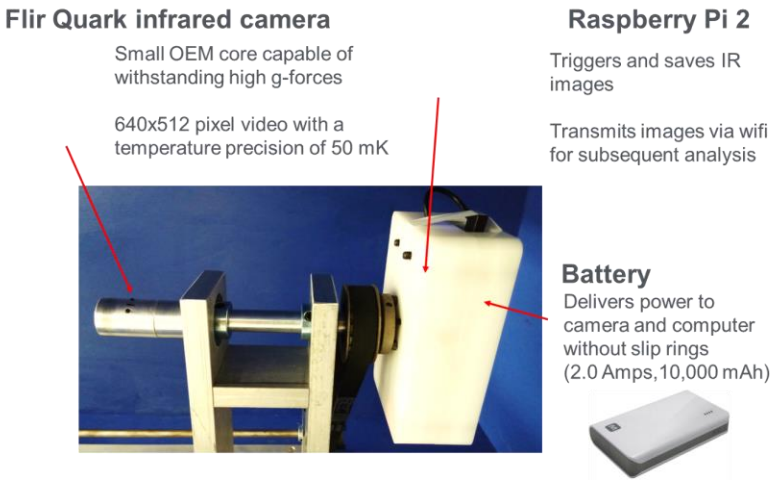

b)

Figure 23. Images showing a) the rotating assembly, which consists of a motor driving both heat transfer body and the infrared thermography system, and b) a close up view of the infrared thermography system.

Experiments were performed with two heat transfer bodies: a three-bladed commercially available propylene fan and an acrylonitrile butadiene styrene disc (0.3 m diameter, 6.35 cm thick). Air-side heat transfer coefficients on rotating discs have been characterized and published in prior literature; the disc was therefore used to validate the methodology used in this work to characterize the heat transfer coefficient. The geometry of the three-blade fan is shown below in Figure 24.

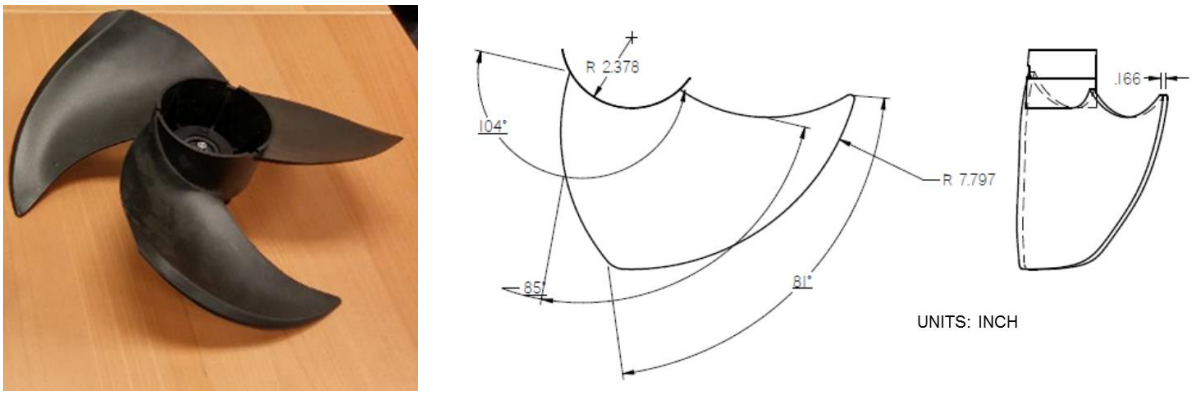

Figure 24. Mechanical drawing of primary fan blade investigated

Table 1 below shows the accuracy of the instrumentation used in the experiments.

Parameter	Instrumentation	Uncertainty	Units
Air temperatures	Omega T-type thermocouple	0.5	K
Surface temperature	FLIR Quark 2 infrared camera	0.6	K
Time	Raspberry Pi computer	0.440	s
Length	Tool Shop caliper	0.01	mm

Experimental procedure

The air-flow heat transfer coefficient was determined for transient cooling. The heat transfer body was first rotated to 863, 1150 and 1725 RPM and then heated to approximately 15 °C above ambient temperature. With the heat transfer body rotating, the heater was then shut off and cooling air was allowed to enter the duct. Data collection and videography was initiated prior to turning the heater off, and the time-stamped temperature data and infrared images were used to characterize the spatial temperature response of the heat transfer body. The region of analysis identified manually for the three-blade fan and with an automatic edge-detection code for fundamental geometries for the disc. The edge-detection scheme used Sobel edge detection in conjunction with a cost minimization routine that identified the mode likely location for the shape of interest. A grid was then formulated within this region; for the three-blade fan, 9801 grid points were arranged so that one dimension consisted of equidistant radial positions and the other dimension consisted of equidistant azimuthal positions between the leading and trailing edges. For the disc, the points were distributed on a grid delineated by polar coordinates. Upon the initiation of cooling, the temperatures these points were recorded, and the corresponding thermal time constants and heat transfer coefficients calculated.

Experimental results and discussion

Validation of experimental methodology

To validate the method of determining the convective heat transfer coefficient through in-situ infrared videography, initial tests were performed with the disc. The results from the tests were compared with convective heat transfer coefficients previously published in literature. Several heat transfer correlations were referenced, expressed in the form of the radial Nusselt number, a non-dimensional convective heat transfer value:

$$Nu_R \equiv \frac{hR}{k}$$

The individual correlations, their heat transfer coefficient predictions and experimental data from the present work are listed in Table 2. Sample thermography images are shown in Figure 24. All correlations are for the average Nusselt number for laminar flow, where the rotational Reynold number, defined in Equation 35 below, is less than 200,000. The Reynolds numbers at the two tested speeds, 863 and 1150 RPM, were 129,719 and 172,768, respectively. While a dependence of the Nusselt number on the Prandtl number (i.e. thermal properties of air) is expected, the Prandtl number is not incorporated in the correlations because they were developed solely for air; the Prandtl number of air is integrated in the constants. It is also useful to note that the dependence of the Nusselt number on the rotational Reynolds number (i.e. exponential) is the same for the rotating disc as that for a flat plate, with the same exponents for laminar and turbulent flows, 0.5 and 0.8 respectively.

$$Re_R \equiv \frac{R^2 \omega \rho}{\mu} \qquad 35$$

Table 2. Heat transfer coefficient correlations for rotating discs with predictions at 863 and 1150 RPM, shown with experimentally measured values from this work.

		Heat transfer coefficient (W/m^2-K) at:	
Study	Correlation	863 RPM	1150 RPM
Cobb and Saunders [26]	$\overline{Nu_R} = 0.36Re^{0.5}$	22.5	25.9
Millsaps and Pohlhausen [27]	$\overline{Nu_R} = 0.28Re^{0.5}$	17.5	20.2
Wagner [28]	$\overline{Nu_R} = 0.335Re^{0.5}$	20.9	24.1
Friction analogy	$\overline{Nu_R} = 0.44Re^{0.5}$	27.5	31.7
Present work (experiment)		23.3	36.1

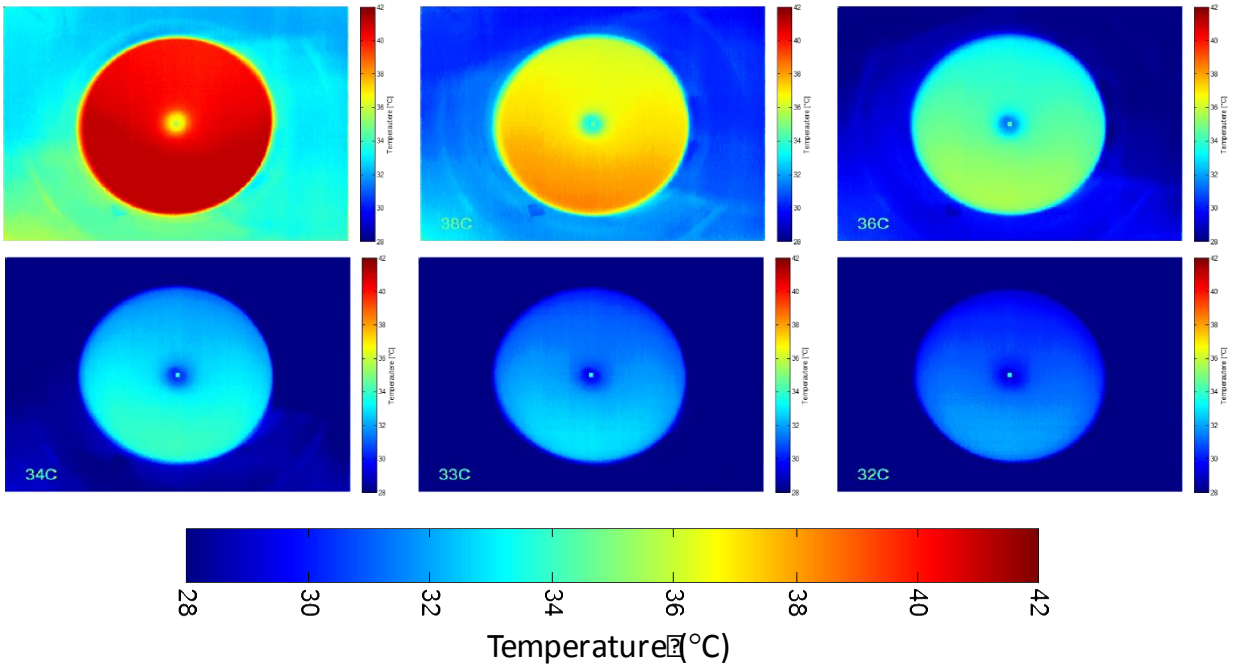

Figure 24. Thermography images of disk rotating at 863 RPM. The sequence of images show the progression of

cooling, from the top left to bottom right at 10 second intervals.

While the experimentally measured heat transfer coefficients are close to those predicted by the correlations, indicating sufficient accuracy, the measured values are slightly higher. This is due to the nature of the experimental setup in this work; a slow axial velocity across the rotating disk was unavoidable. The effect of the axial velocity was assessed by performing a test with no rotation and evaluating the corresponding average heat transfer coefficient. This value, measured to be 25.8 W/m^2-K, was then subtracted from the measurements at 863 and 1150 RPM; the difference is listed in Table 2. However, subtraction is not a complete correction, as it does not fully represent the effect of the axial velocity on the fluid mechanics and heat transfer. It is expected, however, that this axial velocity will be overwhelmed by the drastically higher axial velocity induced by the fan blade used as the actual heat transfer body, and thus will have negligible effect on the results.

Thermal characterization of the three-blade fan

The thermal images of the three-blade fan are shown in Figure 25. The temperature decay characteristics of the individual grid points were then determined; Figure 26 shows a representative decay plot. (While Figure 26 shows spatially averaged decay curves, those of the individual grid points show similar characteristics.) The heat transfer coefficient was subsequently determined from the decay time constant; the local coefficients for clockwise rotation at 1725 RPM is shown in Figure 27.

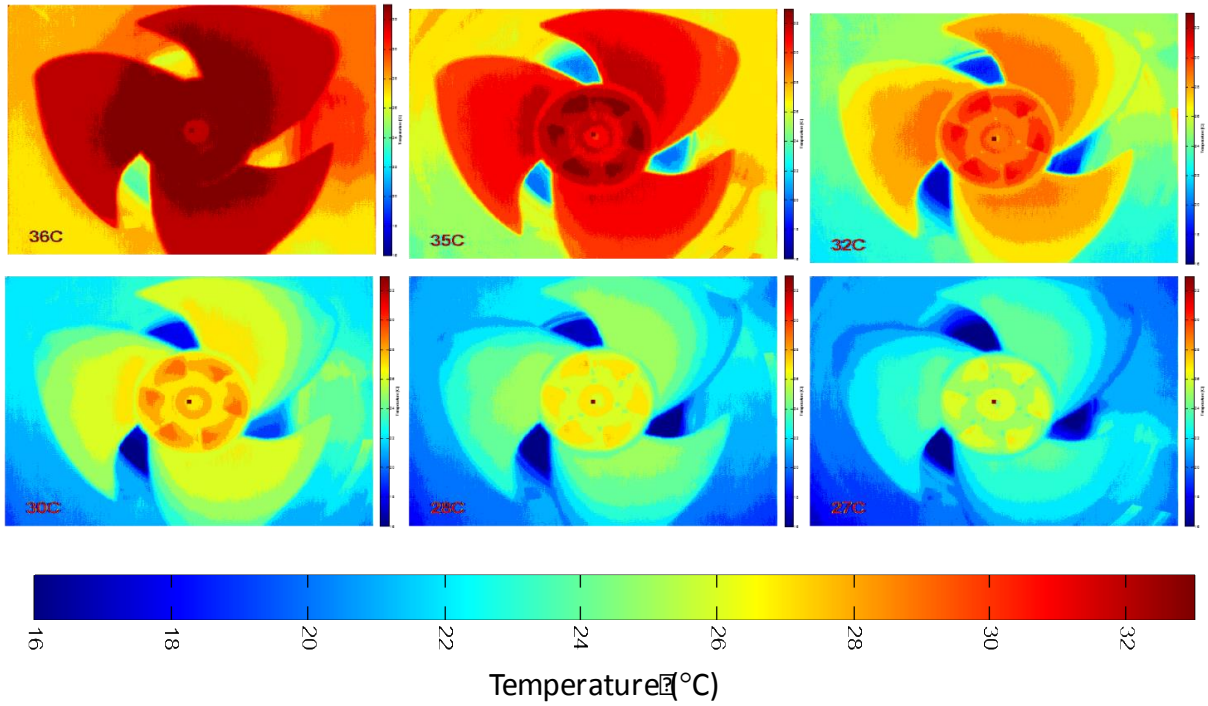

Figure 25. Temperatures of three-blade fan rotating clockwise at 863 RPM. The sequence of images show the progression of cooling, from the top left to bottom right at 10 second intervals.

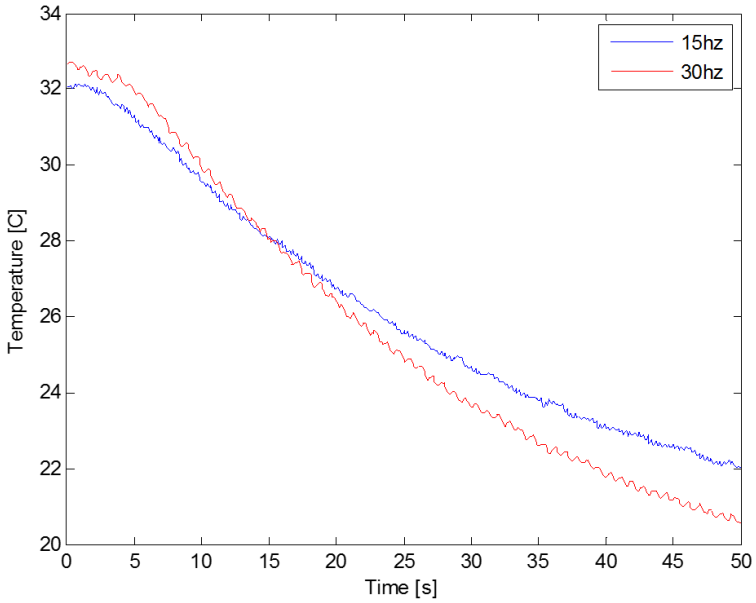

Figure 26. Decay of spatially-averaged temperature of three-blade fan at two speeds, 863 and 1725 RPM.

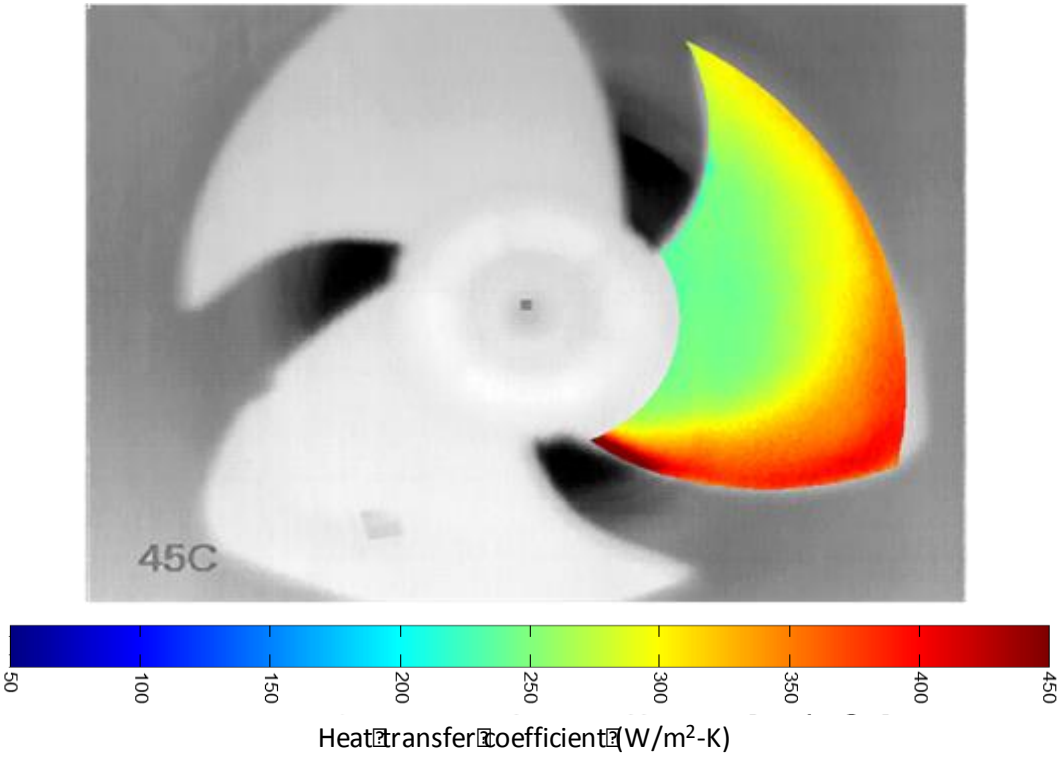

Figure 27. Local heat transfer coefficient at 1725 RPM, clockwise rotation. The heat transfer map is superposed on an infrared image to show orientation.

Figure 27 shows several characteristics of the local heat transfer coefficient. (The region near the hub with nominally high heat transfer coefficient is due to an error in processing and will not be referenced in the discussion below.) First, the coefficient is highest at the leading edge. This is expected, as the

thermal boundary layer develops from the leading edge and becomes thicker away from it. This is phenomenologically the same as forced (parallel-flow) convection on a flat plate, where the highest heat transfer coefficient occurs at the leading edge. Second, for a given azimuthal distance from the leading edge, the heat transfer coefficient is higher at larger radii. The boundary layer growth away from the leading edge, in the azimuthal direction, is retarded at further radial locations due to the higher velocities. Thirdly, sudden spatial changes in heat transfer coefficient are not present. This suggests that transition to turbulent flow did not occur for the conditions tested. While these general trends can be predicted using conceptual framework developed for forced convection in the stationary frame, the effect of the added accelerations unique to the rotating frame is not as clear by simply viewing the plot of local heat transfer coefficients.

From the above observations, it is clear that the local heat transfer coefficient has a functional dependence on both radius and chord length (or equivalently, azimuthal angle for a given radius). Consequently, the Nusselt number was not able to be empirically characterized using only the rotational Reynolds number (defined in Equation 35) or the chord Reynolds number. The chord Reynolds number (Re_C) is defined below, where α is the azimuthal angle from the leading edge and $R\alpha$ is thus the chord length.

$$Re_C \equiv \frac{R^2 \omega \alpha \rho}{\mu} \tag{36}$$

Consequently, for this work, a combinatorial length scale (L) incorporating both radius and chord was used in non-dimensionalization, where

$$L = R + 1.4R\alpha \tag{37}$$

$$Re_L \equiv \frac{R\omega(R + 1.4R\alpha)\rho}{\mu} = \frac{R^2(1 + 1.4\alpha)\omega\rho}{\mu} \tag{38}$$

$$Nu_L \equiv \frac{hL}{k} = \frac{h(R + 1.4R\alpha)}{k} \tag{39}$$

resulting in the following empirical formulation of the local heat transfer coefficient:

$$Nu_L = 0.906 Re_L^{0.64} \tag{40}$$

As only air was tested as the heat transfer medium, the Prandtl number dependence is included in the multiplicative coefficient; the appropriate scaling will be necessary to adapt this correlation to other fluids.

The accuracy of local heat transfer coefficient prediction using Equation 40 is shown in Figure 28 (right column) as side-by-side comparison to the experimental data (left column). Equation 40 captures the spatial gradients of the heat transfer coefficient as well as its magnitude, especially at lower rotational speeds. At 1725 RPM, however, Equation 40 over-predicts the value of the heat transfer coefficient at higher radii and near the leading edge. For reference, the over-prediction is shown in Figure 29. The greatest difference occurs at higher radii, and results in an error of approximately 15%.

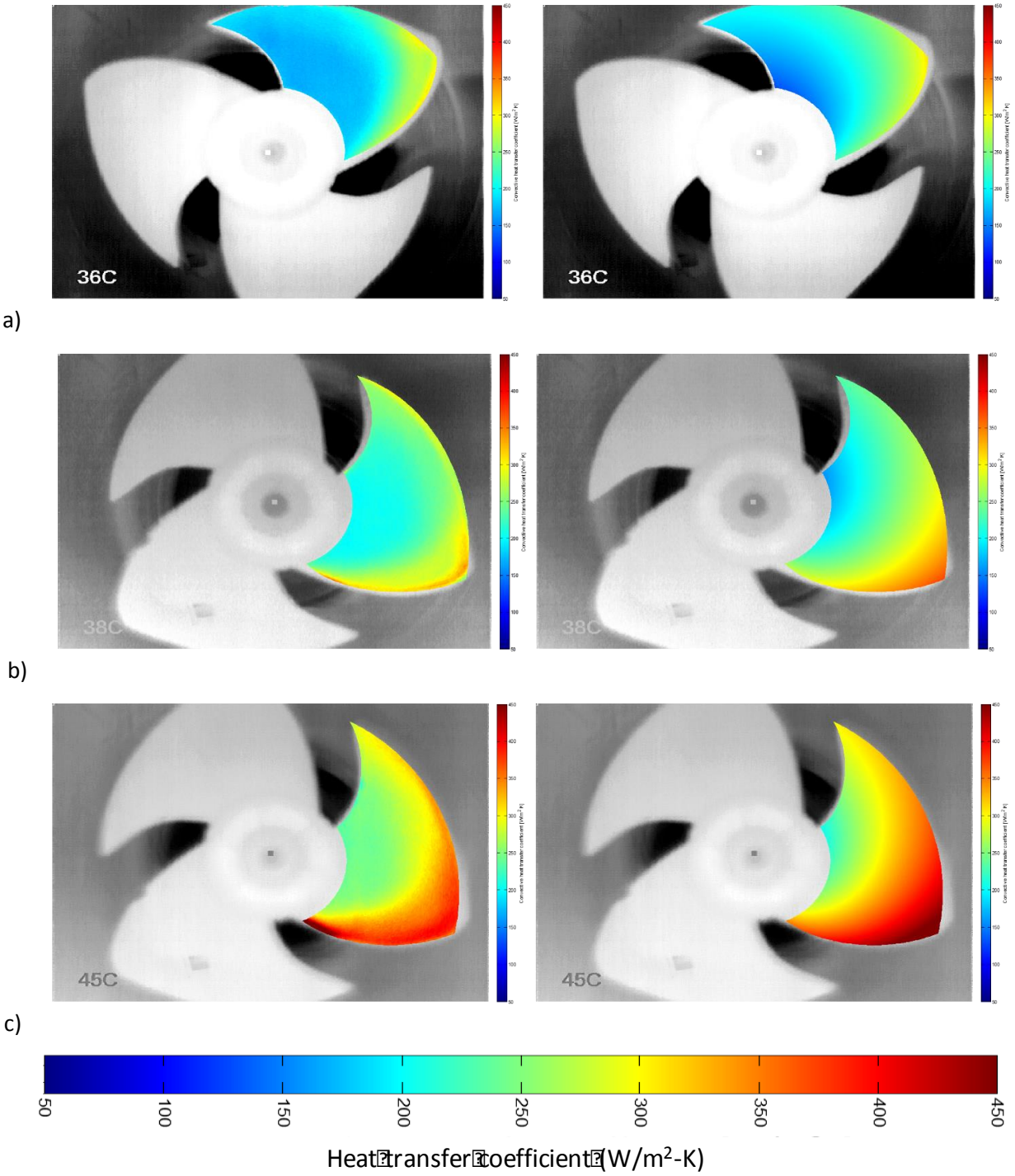

Figure 28. Local heat transfer coefficients at a) 863 RPM, b) 1150 RPM and c) 1725 RPM. For each speed, the left image corresponds to the experimental data and the right to the prediction from Equation 40.

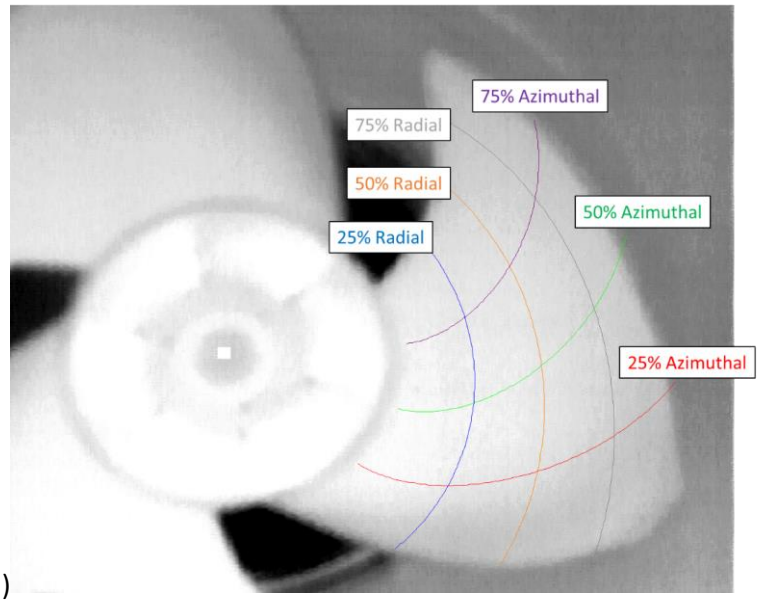
75% Azimuthal
75% Radial
50% Radial
50% Azimuthal
25% Radial
25% Azimuthal

a)

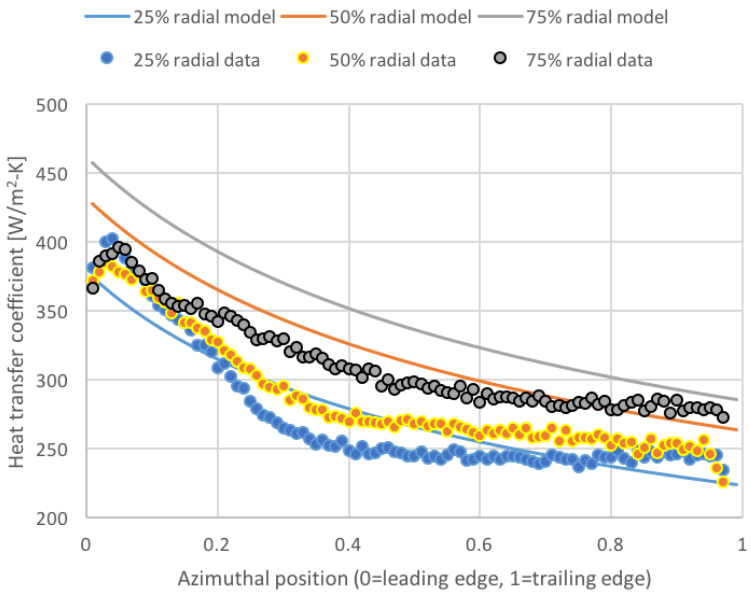
25% radial model
50% radial model
75% radial model
25% radial data
50% radial data
75% radial data
Heat transfer coefficient [W/m²-K]
500
450
400
350
300
250
200
0
0.2
0.4
0.6
0.8
1
Azimuthal position (0=leading edge, 1=trailing edge)

b)

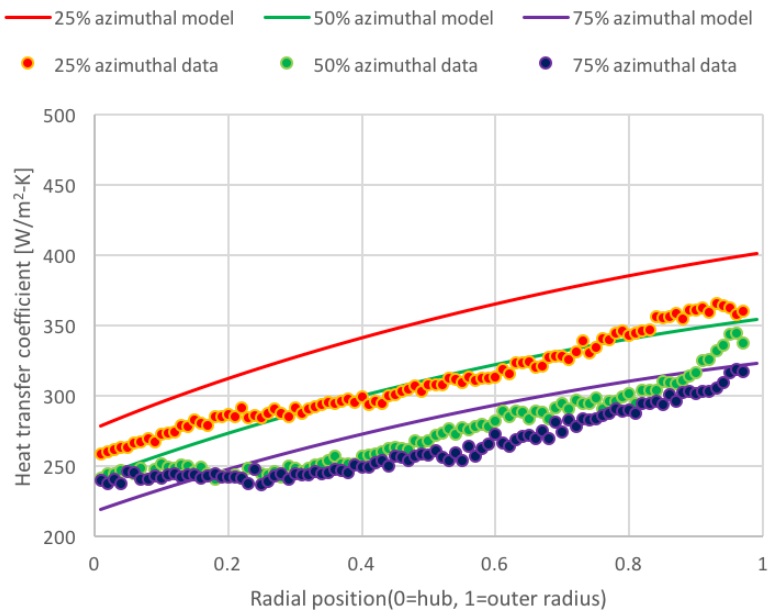

c)

Figure 29. Comparison of local heat transfer coefficients predicted by empirical formula and from experiments, at 1725 RPM, clockwise rotation. a) shows the nomenclature of blade locations. b) shows a sweep of the azimuthal position and c) shows that for radial position.

Prediction of the average heat transfer coefficient is shown in Figure 30. The average heat transfer coefficient was calculated for both experimental and empirical prediction by dividing the area-integral of the local heat flux (total heat transfer) by the total blade area. The shape of the curve in Figure 30 reflects the 0.64 exponent in Equation 38, which, for the limited number of speeds tested, appears to be constant. This exponent is greater than that for laminar, parallel flow across a flat plate in the stationary frame (exponent=0.5), which becomes turbulent (exponent=0.8) when the Reynolds number approaches 500,000 [11]. As the length scale used in the Reynolds number for flat plates is the distance from the leading edge, the chord Reynolds number used in this work is comparable. The chord Reynolds number at 863 and 1150 RPM fall below 500,000, and at 1725 RPM reaches a maximum of 640,000 at the trailing edge. However, as can be seen in Figure 28c and 29b, there is no discontinuity in the heat transfer coefficient towards the trailing edge at 1725 RPM that is characteristic of a laminar-turbulent transition. It is noted that the stationary-frame flat plate is used as comparison for laminar-turbulent transition because the transition on rotating bodies is strongly affected by their cross-sectional profile and is often case-specific. For the same reason, the shape of the rotating blade used in this study (while being constant thickness) could have affected the transition to occur earlier or later. Yet, the Reynolds number exponent, 0.64, appears to be constant and applies throughout the speeds tested as well as the entire blade chord length, which suggests that turbulent transition has yet to take place and thus a heat transfer enhancement is achieved over the stationary frame (exponent=0.5).

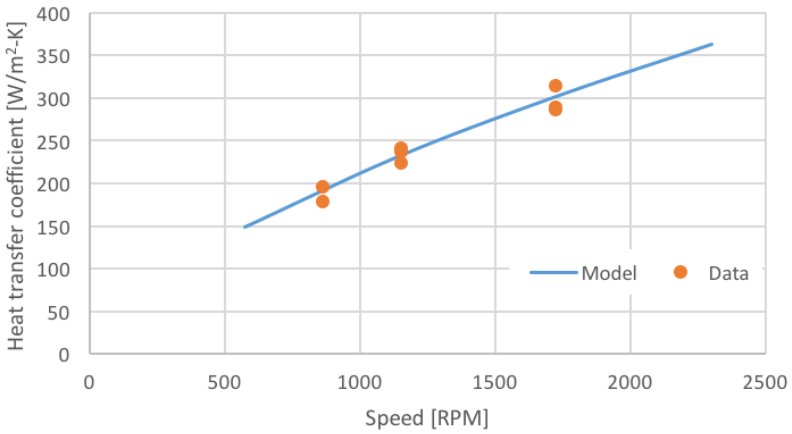

Figure 30. Comparison of average heat transfer coefficient predicted by empirical formula and from experiments.

Figure 31 shows a ratio of heat transfer coefficients (rotating divided by stationary) to directly compare the coefficients. The coefficient is noticeably improved in the rotating frame, especially at the inner radii (lower Reynolds numbers). The improvement at lower Reynolds number suggests that the laminar boundary layer is thinner in the rotating frame, consistent with prior work [12, 13].

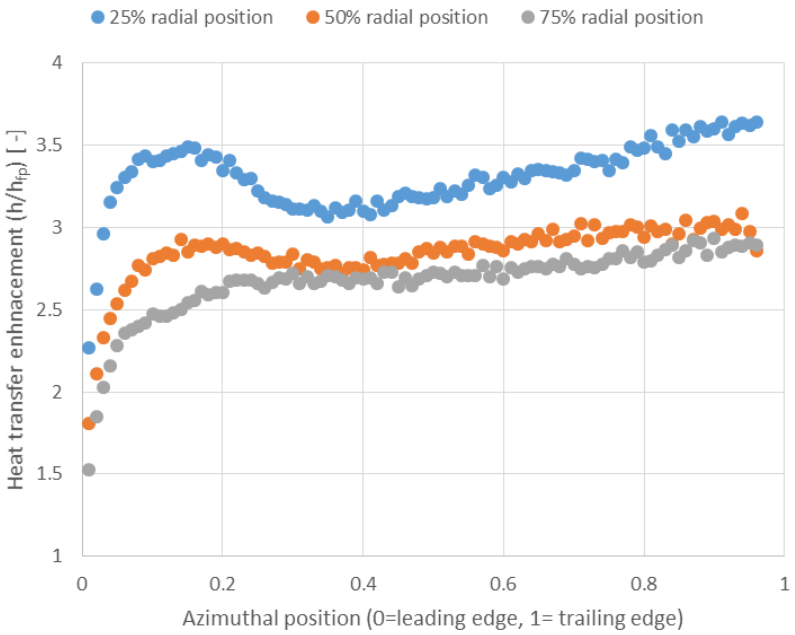

Figure 31. Heat transfer enhancement in the rotating frame, showing the ratio of heat transfer coefficients (rotating divided by stationary). The stationary case is a parallel flow stationary plate. The azimuthal position corresponds to the distance from the leading edge for the stationary case and the radial position represents the corresponding air velocities.

Summary of results

The results from the air-side investigation provide the following insights.

1) First, and most importantly, a substantial heat transfer enhancement (250-350%) is achieved in the rotating frame without noticeable transition to turbulent flow. The enhancement is not conditional or locational, but occurs through all conditions tested, throughout the blade. This enhancement is pivotal for the viability of the RVCC concept.
2) Second, the highest heat transfer coefficients are achieved near the leading edge. Therefore, for a given total blade area, the average heat transfer coefficient can be increased by employing more blades with shorter chord length.

6. Heat Transfer and Pressure Drop through Rotating Fins

The experimental results from the previous section indicate promising heat transfer coefficient improvement in the rotating frame for a bare heat transfer blade. The RVCC topology may offer efficiency benefits for applications where the blade surface area is sufficient for the total heat load. For heat transfer magnitudes on the order of a commercial air-conditioning / heating unit (5+ tons), heat transfer surface area enhancements, such as fins, may become necessary for the RVCC layout to increase efficiency beyond that of the current state-of the-art (STOA) unit. Namely, this is because the STOA units largely increase their efficiencies by utilizing heat exchangers with higher surface areas.

For reference, a current STOA 5-7 ton air conditioning unit incorporates a condenser with a frontal area of approximately 1 m by 2-3 m, with substantial finning. Nearly all commercially available condensers can be categorized in two main types, 1) finned round tubes or 2) finned "microchannels" (Figure 32). Microchannels are a linear bundle of channels, which have a hydraulic diameter on the order of a millimeter, in a single planar aluminum extrusion. Variations among the round tube designs generally come in the form of the different fin structures. All American HVAC companies, with the exception of Trane, utilize a plate fin structure, where multiple tubes run through the tight-fitting holes cut into the fin sheet. Typical fin pitch thickness ranges from range from 0.1 to 0.16 mm, and fin pitch ranges from 2 to 1.25 mm (12-20 fins per inch). Trane uses "spline fins," where the fins approximately appear like the bristles on a bottle or pipe cleaner, with the pipe as the axis. In this design, fin pitch is more difficult to characterize, as the fins are spread randomly but tightly around the tube. It is important to note that both round tube designs are strongly dictated by economical manufacturability. Microchannel heat exchangers, on the other hand, are more costly to manufacture and therefore have had limited market penetration. They typically have a folded array of planar fins between the adjacent microchannel extrusions (Figure 32). The plate fins on both tube types can be louvered.

a) 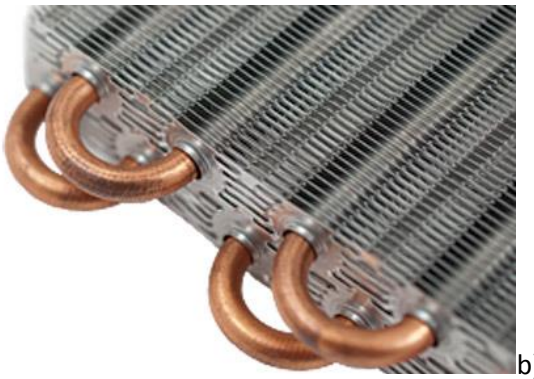 b) 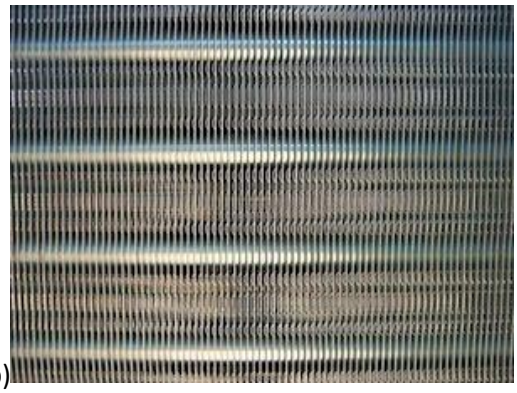

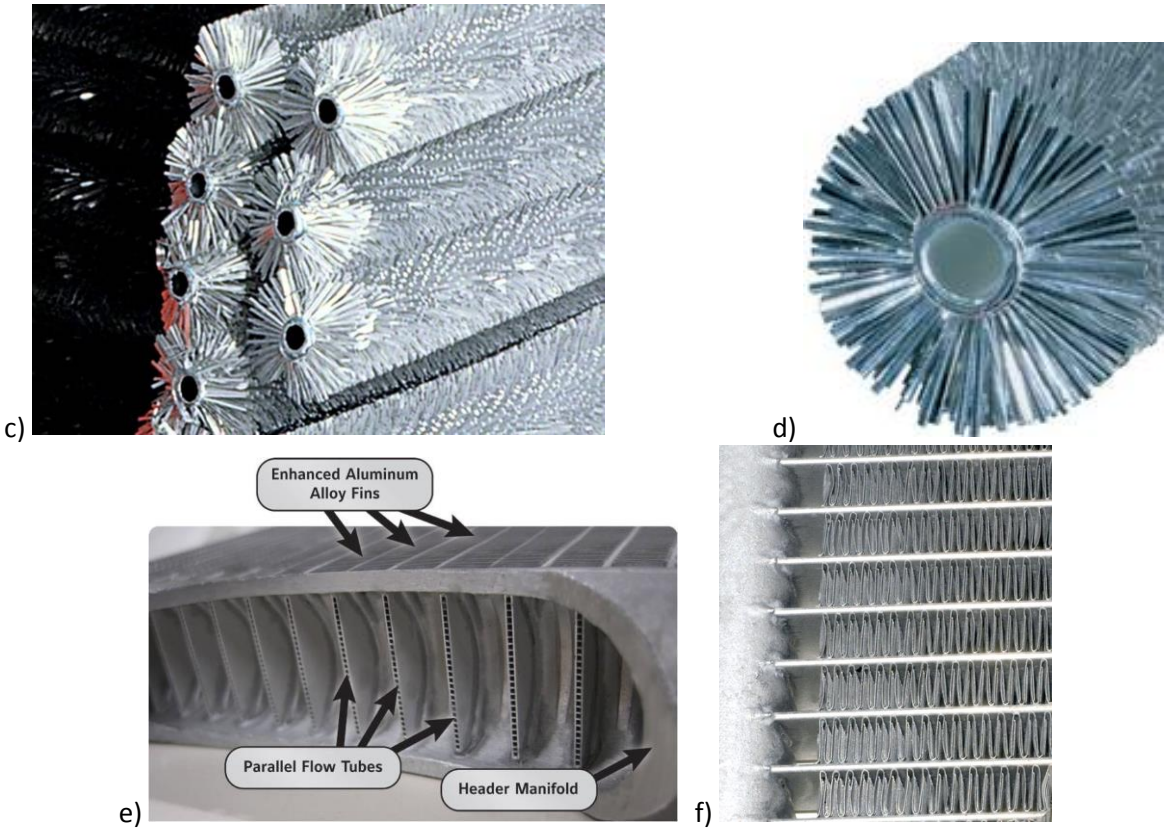

Figure 32. Air-cooled heat exchanger designs used in commercially available air-conditioner units. (a)-(d) show round tube designs. (a) and (b) show the different views of the plate-fin round tube design; louvers can be seen in the fins in (a) [6, 29]. (c) and (d) show a bank and a single tube, respectively, the spline-fin design. (e) and (f) show the microchannel design [7, 30]. (e) is a cut-away view inside the header, showing array of microchannels, and (f) shows the planar fins in a frontal view of the microchannel heat exchanger [10].

As the heat exchangers are rotated in the RVCC layout, there is a limit to their size. Larger rotating bodies are more sensitive to imbalances, resulting in higher manufacturing cost and maintenance. The heat exchangers for the RVCC topology will therefore need to be smaller in size than those of a stationary STOA unit with equivalent cooling/heating capacity. This downsizing is only possible with substantially enhanced heat transfer. While the addition of fins helps this, dense fin packing will increase the frictional losses associated with the air flow. This is exacerbated in the rotating frame due to the significantly higher relative velocity between the heat exchanger and air. It is therefore possible that the higher power consumption associated with generating the air flow nullifies the benefits afforded by the enhanced heat transfer. To summarize the design constraints on the RVCC heat exchangers,

1) The heat exchangers must be substantially smaller that the STOA stationary counterpart. (e.g. 1 m diameter maximum).
2) Despite the smaller size, the heat exchangers must have lower thermal resistance than the STOA stationary counterpart, otherwise the RVCC topology will not afford any performance/energy efficiency gains over the current STOA air-conditioner/heater.
3) Due to 1 and 2 above, fins are necessary to increase area and achieve the necessary heat transfer performance. However, they cannot have the same density as the STOA stationary heat

exchangers. The high relative velocity in the rotating frame will increase the air-flow pressure drop across the heat exchanger to unacceptable levels.

This portion of the study focuses on part 3 above, and investigates the air-side heat transfer and flow characteristics on representative fins structures in the rotating frame. Emphasis will be placed on the tradeoff between the two, and how that compares to that of existing stationary heat exchangers.

Model Details

Due to the difficulty in developing a representative experiment without the fabrication of an entire device, the characteristics of the rotating heat exchanger was analyzed using computational fluid dynamics. Specifically, it is difficult to create the air-flow losses at the entry and exit of the flow channel between the fins while taking into account the influence of the air flow into the neighboring channels. The general design of the rotating heat exchanger modeled is shown in Figure 33 below. The finning structures are connected to the hollow refrigerant blades, and occupy the inter-blade spaces. The fins adopt the angle of the blades, which is constant and sets the ratio between axial and tangential velocities of the relative air velocity.

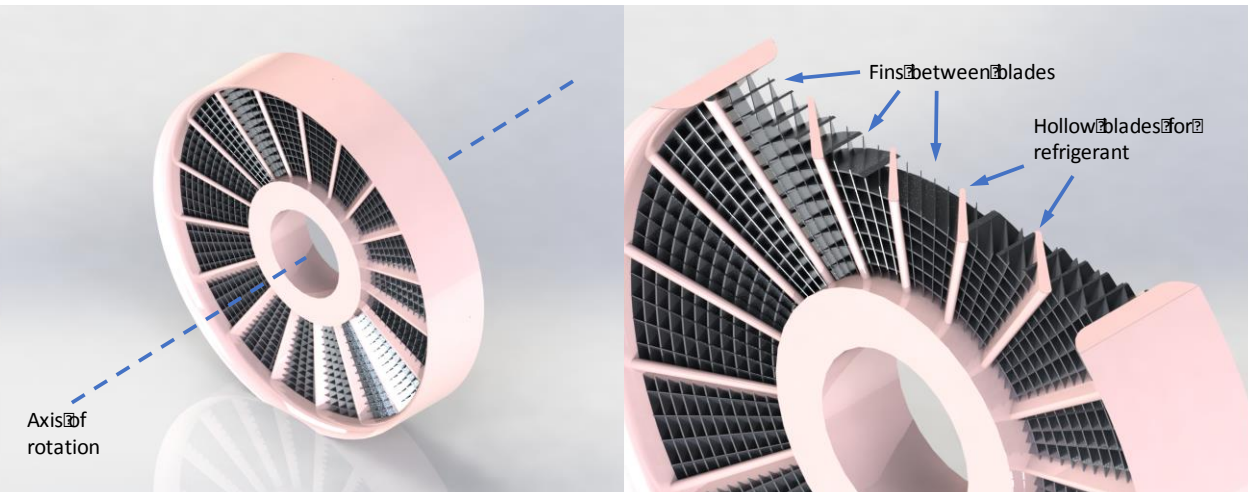

Figure 33. Rotating heat exchanger topology modeled in computational fluid dynamics. In this diagram, the heat exchanger rotates clockwise. The light pink regions represent the hollow body housing the refrigerant, consisting of the inner and outer annuli, connected by the hollow heat transfer blades. The fins structures branch off of the blades and occupy the inter-blade spaces. The axial flow length shown here is shorter than that shown in the schematic shown in Figure 7.

Computational modeling was performed with ANSYS CFX to solve the combined heat transfer and fluid mechanical differential equations. A representative modeled geometry is shown in Figure 34; the net air flow is axial. At the center region is a bundle of channels with a constant pitch angle; two stacked sectors above and below the channels represent the inlet and outlet air regions, respectively. The channels represent the flow space between the fins. The center axis of the sectors is the center of rotation. As the pitch angle is constant, it can be described by the axial rise over the azimuthal run. Rotationally periodic boundary conditions were imposed on all azimuthal boundaries to simplify the calculations. The bundle of channels is centered on a radial row of three channels, with rows of half channels on the azimuthal fore and aft sides of the full channels. Rotationally periodic boundary conditions were imposed on the open ends of the half channels. The temperature of the four walls of

the center channel was set to be 45 degrees C and the inlet air temperature was set to 35 degrees C (for a similar temperature range to the conditions of ANSI/AHRI Standard 210/240); unrealistic buoyancy effects due to high temperature gradients were therefore avoided. To ease computation, only the center channel is diabatic and all heat transfer characterization is performed on that channel. The neighboring channels are included in the model to more realistically represent the fluid flow into the center channel. While the isothermal surface condition facilitates computation, it does not include the conductive losses in the fin bodies; to account for this, the heat transfer coefficient (model output) was scaled down using the fin efficiency determined for a 0.1 mm plate fin thickness. The two stacked sectors at the inlet and outlet are used to capture the two frames; one is in the stationary frame and the other is in the rotating frame, with the interface between the two modeled with frozen rotor. Consequently, from the inlet to the outlet, the model regions are: stationary inlet sector, rotating inlet sector, rotating channels, rotating outlet sector and stationary outlet sector.

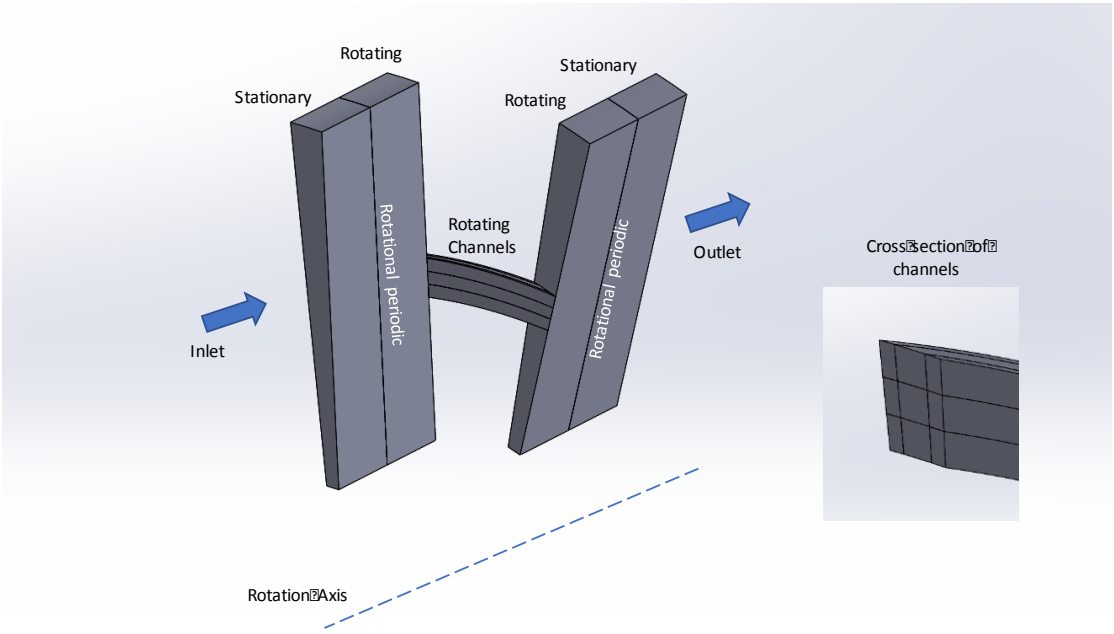

Figure 34. Regions modeled in computational fluid dynamics. A bundle of nine channels represents the inter-fin air-flow space; the walls of the center channel are diabatic. The nine channels are independent and separated by walls. The angle of the channels is equivalent to the angle of the blades in Figure 33. The different frames (stationary and rotating) are accommodated using different regions for each frame, with a frozen rotor boundary at the frame interface. All azimuthal faces are modeled with rotational periodicity, and all boundaries besides the inlet, outlet, and region interfaces are solid walls.

The inlet and outlet boundaries were modeled as openings at atmospheric pressure such that the rotation of the heat exchanger drove the air flow. Due to the constant pitch angle, the axial air flow velocity through the channel was a fixed fraction of the tangential speed. Local deviation occurred from this velocity, due to viscous effects within the channel.

Modeling was performed with the center channel at a radial distance of 30 cm from the center axis, at rotational speeds of 50 rad/s, 75 rad/s and 100 rad/s. The channels were modeled with two cross sectional areas, 1 cm x 1 cm and 0.5 cm x 1 cm (tangential x radial length). Various rise x run combinations were modeled; the 1 cm x 1 cm channel was modeled with 1 x 3, 1 x 4, 2 x 4, 2 x 6, 2 x 8 and 3 x 6 pitches (units: cm x cm), and the 0.5 cm x 1 cm channel was modeled with 1 x 2, 2 x 4, 1 x 3, 1 x 4, and 2 x 6 pitches. These pitches correspond to angles of 14.0°, 18.4°, and 26.6°.

Analysis Methodology

Analysis of thermal and frictional performance of air-cooled heat exchangers is a well-studied subject. Kays and London have published a seminal compilation of an exhaustive list of experimental data on heat exchangers, and more recently, Wang and Chang's group has made Nusselt number and Friction factor correlations using a substantial body of experimental data using their own as well as those of past researchers [31-33]. However, Wang and Chang base their results on a Reynolds number using a dimension specific to particular types of heat exchangers, limiting their generality. Therefore in this analysis, the performance of the modeled RVCC heat exchanger will be compared to the data from Kays and London [34]. For the RVCC concept to be viable, the thermal performance of the rotating heat exchangers must be better than that of existing heat exchangers by the multiplicative factor that the heat exchangers have to be downsized by to be rotatable.

Comparison will be made on the basis on two non-dimensional numbers. To characterize heat transfer, the Colburn J-factor is used

$$j = StPr^{2/3} \tag{41}$$

which is a function of the Stanton number,

$$St = \frac{Nu}{Re_{axial}Pr} = \frac{h}{\rho V_{axial} C_p} \tag{42}$$

As the cooling medium is always air and the Prandtl number hardly changes in the range of air temperatures considered (for the condenser), the J-factor can be considered to be the Stanton number multiplied by an approximate constant. In heat exchanger analysis, the Stanton number is a more holistic metric than the Nusselt number, as it describes how well heat is transferred for a given air velocity. The Stanton number has a functional similarity to the Number of Transfer Units used in heat exchanger characterization, and enables the normalization of heat transfer performance despite different flow lengths. This characteristic allows for the comparison of different heat exchanger geometries using the same metric. To retain this functional similarity, the Reynolds and Stanton number are calculated with the axial velocity, which is associated with the net mass flow rate through the heat exchanger. The relative velocity is the vector sum of the axial velocity and tangential velocity of the fin structure due to rotation, where the ratio of the axial and tangential velocities is determined by the fin angle.

To characterize frictional losses, the friction factor is used, as defined by Kays and London [34],

$$f = \frac{A_c \rho_m}{A \rho_i}\left[\Delta P \frac{2g}{V^2 \rho_i} - (1+\sigma^2)\left(\frac{\rho_i}{\rho_o} - 1\right)\right] \tag{43}$$

where ΔP is the pressure drop across the heat exchanger. A_C is the constricted free-flow area (open area between the fins) and A is the total heat transfer area. The ratio of the two can be interpreted as a method of translating pressure drop to an effective wall shear. σ is the ratio between A_C and the total frontal area (equal or less than unity) and g is the gravitational acceleration. The subscripts i and o refer to the inlet and outlet of the heat exchanger and m indicates the arithmetic mean of the inlet and outlet. The first term in the parenthesis represents the flow friction and the second term represents the flow acceleration. While the effect of acceleration is removed from the friction factor, this definition

still includes the effects of the entry and exit pressure losses. For consistency with previous analyses, the friction factor will be assessed in the rotating frame such that the channel appears stationary with air flowing through it at the relative velocity. Note that this definition by Kays and London is different from that used elsewhere due to the inclusion of g, which is treated by as a non-dimensional constant.
In this study, the friction factor is treated as a *non-dimensional mechanical cost* of air flow, where the pressure drop is the potential necessary for the flow that results in power consumption. Considering the air flow through a stationary heat exchanger,

$$Mechanical\ power\ consumption = W = \Delta P\dot{V} = \Delta P A_c V \quad (44)$$

where the $\dot{V}$ is the volume flow rate and V is the velocity used In Equation 42. Note that this pressure drop is due to any mode of flow resistance, (body drag, shear drag as well as entry and exit losses) and is not solely due to viscous shear at the surfaces.

In the rotating heat exchanger, the power consumption can come from two sources 1) from the generation of the air flow, and 2) from the torque necessary to spin the rotating heat exchanger. The two can be decoupled to an extent by having a dedicated fan blow air axially at the rotating heat exchanger. Alternatively, as modeled in this study, the rotating heat exchanger can serve as the fan, generating its own air flow. The torque is unique to the rotary configuration, and therefore has not been encountered in previous heat exchanger studies. In order to make a fair comparison using the established friction factor metric, the two above components are incorporated into the friction factor on the basis of energy consumption.

The total energy consumption associated with the rotating channel is calculated via total enthalpy change across the channel, from which the effective pressure drop is calculated using Equation 44.

$$Mechanical\ power\ consumption = \Delta Total\ enthalpy - Heat\ input \quad (45)$$

$$\Delta P_{effective} = \frac{Mechanical\ power\ consumption}{\dot{m}_{net}/\rho} \quad (46)$$

where $\dot{m}_{net}$ is the net mass flow rate of the air. The effective pressure drop includes body and shear drag, inlet and exit losses, as well as the angular momentum transfer to the air flow, and is on the order of the difference between the highest and lowest pressures in the flow.

Results

Section 2 reported heat transfer improvements in the rotating frame for a non-finned blade. Figure 35 shows a similar enhancement in for the finned case, where the heat transfer in the rotating and stationary frames are compared based on the Nusselt number as a function of the Reynolds number. Both non-dimensional numbers are defined with the hydraulic diameter of the channel, and the relative velocity is used for the Reynolds number to take into account the nature of the interaction between the air and fins. The Nusselt number for channel flow in the stationary frame was estimated using Gnielinski's formula [16]. The heat transfer is enhanced in the rotating frame, gradually increasing with Reynolds number to an approximate 40% increase at 19,000. In the rotating frame, the Nusselt number is approximately linearly dependent on the Reynolds number, in contrast to the 0.8 power dependence on Reynolds number in the stationary frame. For reference, for the 1 cm x 1 cm channel, the heat

transfer coefficients at 50, 75 and 100 rad/s are approximately 90, 140 and 180 W/m^{2}K.

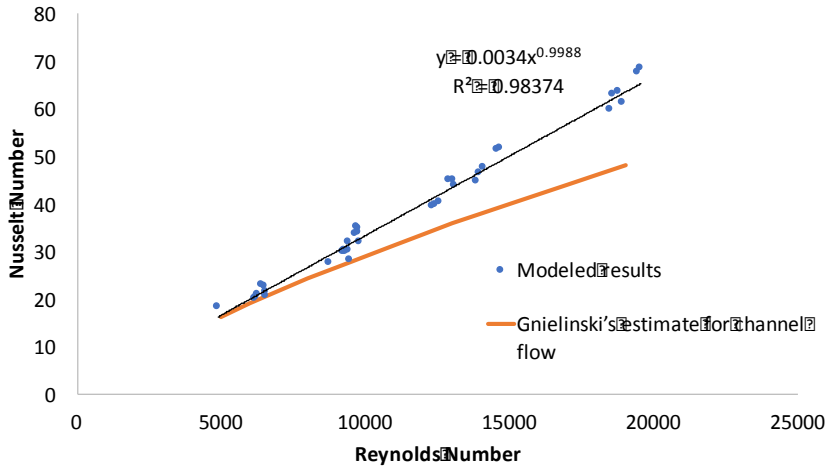

Figure 35. Nusselt number as a function of Reynolds number, comparing CFD results and channel flow estimates using Gnielinski's formula [16].

Figure 36, 37 and 38 shows the J-factor as a function of the friction factor. These plots show the tradeoff between the heat transfer performance and frictional flow resistance. Figure 36 shows this for existing air-cooled heat exchangers using data from Kays and London; for consistency and clarity, the same nomenclature are used as in the text. (The data points for the "plate fin round tube" design were manually taken from a graph in the text, all others reference tabulated data.) The most basic variant of the current STOA round tube condenser is represented by the "plate fin round tube" design with straight fins (no louvering or wavy fin forms, hence representing the lowest friction variant). As most microchannel heat exchangers use planar louvered fins, it is represented by the "louvered plate fin." "Banked finned tubes," "strip fin plate fin" and "wavy fin," (shown in Appendix B) and are also included in Figure 36 as their fin geometries can be incorporated fairly easily to round tube and microchannel heat exchanger designs. Banked finned tubes consist of a set of spaced parallel tubes, similar to the plate fin round tube design, but use individually stamped round sheet metal collars slipped over the tubes. Strip fin plate fins are similar to simple plate fin designs, but use multiple staggered plate strips. Wavy fin plate fins are a variant of the plate fin design where the plates have bends orthogonal to the direction of the flow (i.e. the bends force the flow to bend as well).

In interpreting Figure 36, it is instructive to note that low Reynolds numbers (flow velocity) result in higher friction factors, so the upper right most points for each data set represent the lowest velocities tested (Reynolds numbers of 300-600). Consequently, any extrapolation of the data sets further into the upper right direction may not be practical. The J-factor decreases as the Reynolds number increases because the Stanton number is a function of the Reynolds number to a negative power. For example, for the laminar flows, the Nusselt number is a constant, independent of the Reynolds number, so the Stanton number is a function of the Reynolds number to the -1 power. Alternatively, for the turbulent case, the Nusselt number is a function of the Reynolds number to the 0.8 power [16], rendering the Stanton number a function of the Reynolds number to the -0.2 power via Equations 41 and 42. It can be seen that the plate fin round tube design has the most advantageous heat transfer-friction relationship, although it has a lower upper bound on J-factor than the other designs. Wave and strip fin plate fin designs offer higher J-factors, although this comes at a higher frictional cost. As the design with the highest J-factor for a given friction factor will be most efficient, the data in Figure 36 can be condensed

into a single frontier plot that represents the best operating points possible from the selected stationary heat exchangers, as shown in Figure 37. Figure 37 also shows the corresponding Nusselt numbers for a Prandtl number of 0.71. Note that the Prandtl number only changes from 0.713 to 0.709 as the air temperature changes from 20° to 60° C.

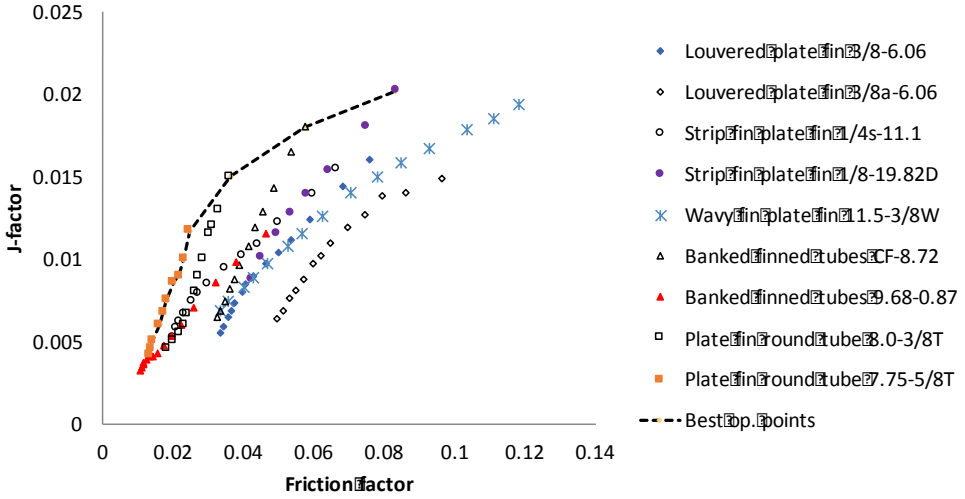

Figure 36. J-factor as a function of friction factor, for various existing air-cooled heat exchanger designs. The nomenclature for the heat exchangers is taken directly from Kays and London [34].

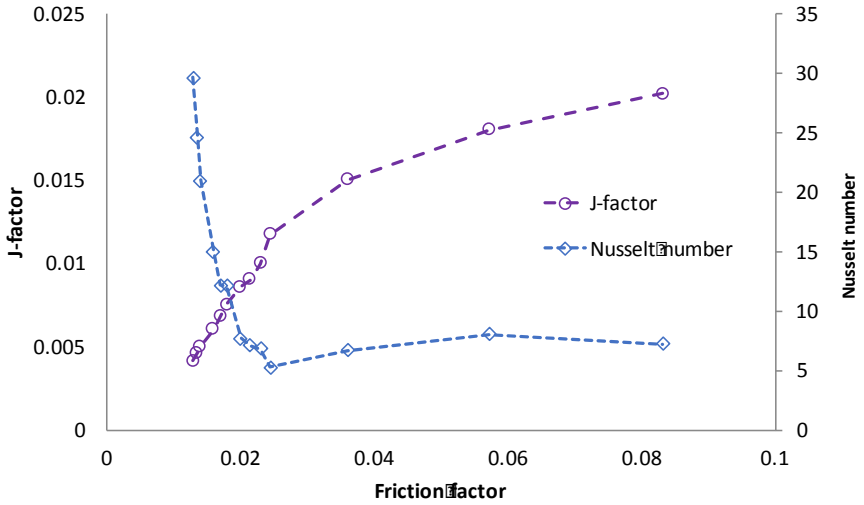

Figure 37. J-factor and Nusselt number as a function of friction factor. The data shown represents the best performance that can be achieved by existing heat exchanger designs; it shows the highest J-factors for a given Friction factor from the data set in Figure 36.

Figure 38 shows the results of the computational modeling. The data is grouped by fin angle, which had the largest influence on the J-factor. The curve from Figure 37 (hereafter, "stationary fins") is also included in the plot for comparison. Due to non-dimensionalization, effects of the cross-sectional flow area and flow length are normalized. The rotating fins has higher Nusselt numbers than the stationary fins, but as this is largely due to the higher relative velocity between the air and the heat exchanger surface (Figure 35 and 37), it has comparable J-factors to stationary fins. The friction factor decreases with rotation speed and Reynolds number. Due to the change in frame and the small but non-negligible

amount of angular momentum imparted on the flow, the rotating fins generally have a higher friction factor than the stationary heat exchangers. Consequently, except for a subset of the modeled conditions which lie to the upper left of the stationary heat exchanger frontier curve, the rotating fins perform less efficiently than stationary fins.

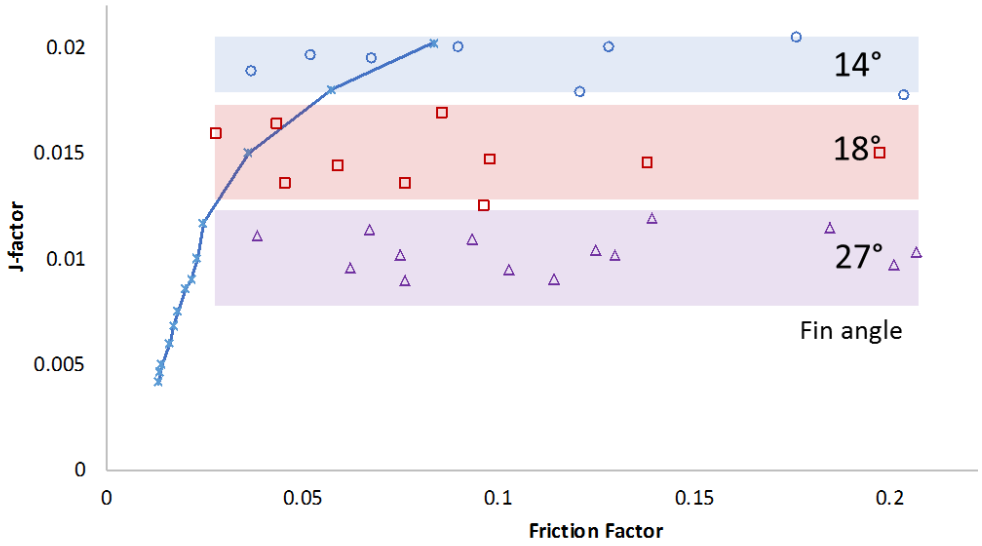

Figure 38. J-factor as a function of friction factor, showing the results from the CFD modeling as well as the best performance curve of existing stationary heat exchanger designs (stationary fins) from Figure 37. The fin angles of the modeled fins are labeled for reference.

In contrast to the decrease in J-factor with increasing Reynolds number and friction factor, the J-factor in the rotating heat exchanger is relatively constant for a given fin angle. This is due to the linear dependence of the Nusselt number on the Reynolds number, making the J-factor approximately a function of the Prandtl number (a material property) to the -1/3 power.

$$j = StPr^{2/3} = \left(\frac{Nu}{Re_{axial}Pr}\right)Pr^{2/3} \approx \frac{Nu}{Const * Re_{relative}}Pr^{-\frac{1}{3}} \approx Const * Pr^{-\frac{1}{3}} \qquad 47$$

where the Reynolds numbers based on the axial and relative velocities are geometrically related through the fin angle. Consequently, while increasing the Reynolds number lowers the friction factor, the J-factor changes little. Higher J-factors occur at lower fin angles, which allow for higher relative velocities and heat transfer coefficients for a given axial velocity. Like the J-factor, the Stanton number is constant as a change in velocity results in an equal change in the heat transfer coefficient. For a given fin temperature, a constant Stanton number means that the air temperature change across the heat exchanger remains constant, independent of the rotation speed.

Practical limits must be considered at low fin angles, however, as the heating (cooling) of the air flow in a condenser (evaporator) must be considered. Overly shallow angles can lead to a low air flow rate, resulting in the air temperature approaching that of the fins, diminishing the temperature difference available to drive the heat transfer.

Figure 39 shows relevant data where the rotating fins perform better than stationary fins. The three points for each fin channel represent three different Reynolds numbers, with the highest speed having the lowest friction factor. The different Reynolds numbers can represent different radial locations on a

single rotating heat exchanger. The rotating heat exchanger thus spans a range of friction factors and the integral sum of the power consumption from must be considered when making a device-level comparison with the stationary heat exchanger. Efforts to shift the range of friction factors leftward invariably lead to larger diameters or faster rotation speed. For the 14 degree fin angle, the critical tangential velocity to perform better than the stationary fin heat exchanger was found to be 23 m/s. Note that the highest tangential velocity modeled was 30 m/s (0.3 m radius at 100 rad/s), weighing realistic limits of cost and safety. Within this constraint, the maximum improvement over stationary fins is on the order of 15% at a fin angle of 14 degrees.

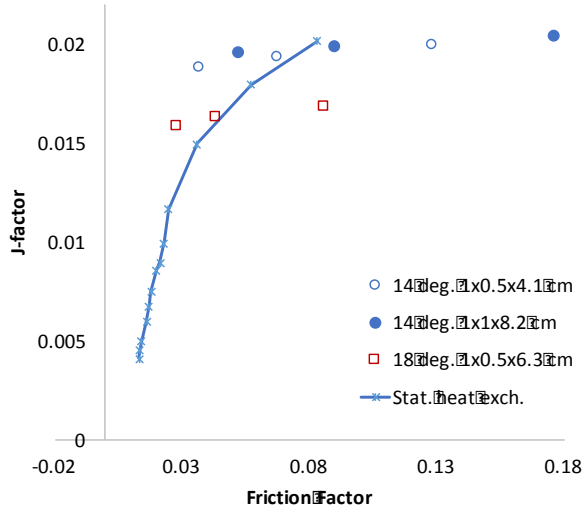

Figure 39. J-factor as a function of friction factor, showing relevant results of the CFD modeling where the performance of the rotating fins exceeds that of the stationary fins. The solid line represents the best performance curve for existing stationary fin heat exchangers, from Figure 37.

Conclusion

Representative rotating heat exchanger fin designs were modeled computationally to assess the heat transfer and flow friction characteristics. The results of the modeling were compared to the performance of various existing air-cooled heat exchanger designs. While the rotating fins can achieve significantly higher convective heat transfer coefficients and Nusselt numbers, it does so at the cost of higher pressure drop. A general comparison of the heat transfer and fluid flow characteristics of the rotating and stationary fin designs was made using the non-dimensional J-factor and friction factor, respectively. While certain fin designs and operating conditions (shallow fin angle and high tangential velocity) resulted in better performance in the rotating fins, the improvement was found to be a maximum of approximately 15%. Consequently, when the remaining engineering risks are considered for the rotating heat exchanger and the RVCC concept, a simpler solution to achieve the same level of improvement may be to increase the size of the heat exchanger by 15%, or by improving the manufacturing technique of the heat exchangers albeit at a higher cost (e.g. brazing or soldering the plate fins to the tubes for better thermal connection).

Summary and Conclusion

The Rotary Vapor Compression Cycle (RVCC) concept was conceived to address several modes of thermodynamic losses inherent in conventional Vapor Compression Cycles (VCC) used for space heating, cooling and refrigeration systems. The concept takes advantage of the heat transfer and anti-fouling benefits pioneered in previous work for a rotating small-scale heat sink [12, 13], and requires the rotation of the entire VCC. Rotation of the VCC potentially offers additional benefits through the use of centrifugal phase separation to prevent liquid ingestion at the compressor as well as to sort the two-phase flow for enhanced vapor escape and consequently, higher heat transfer coefficient.

This project was the first step in developing the RVCC concept, and focused on addressing the highest level risks associated with the technology, which were:

- On the refrigerant side, the ability to implement the VCC in the rotating frame and understanding its operating characteristics.
- On the air-side, understanding the magnitude of the air-side heat transfer enhancement achievable in the rotating frame and the associated pressure drop penalty when finning structures are used for surface area enhancement.

Consequently, this project was structured in the following parts. First, the applicability of the VCC in the rotating frame and the characteristics of refrigerant distribution in the rotating frame were studied. Second, the spatial variance of the air-side heat transfer coefficient on un-finned rotating bodies, as well as the magnitude of improvement over that in the stationary frame, were investigated. Lastly, the tradeoff between heat transfer improvement and pressure drop increase due to the use of finning structures on the rotating bodies was assessed.

The refrigerant-side study was performed using a prototype rotating VCC with transparent windows in the evaporator and condenser for visual access to the two phase flow and liquid distribution. The response of the saturation pressures to changes in refrigerant mass flow rate showed that the VCC was operating properly. Centrifugal separation of the vapor and liquid phases was observed in the evaporator, condenser and the passage to the compressor. Higher centrifugal acceleration at higher rotation speeds resulted in the thinning of the condensate film in the condenser and thus lower system thermal resistance. Despite this, centrifugal acceleration-propelled refrigerant flow was found to have limitations; centrifugal acceleration was not sufficient to supply the evaporator channels with enough liquid or to thin the condensate film. Consequently, the evaporator channels were under-occupied by liquid and the thermal resistance in the condenser was high, and centrifugal acceleration was not found to be an effective means of generating refrigerant flow in the channels. To avoid these drawbacks, evaporator and condenser channel designs that use the more conventional pressure-driven flow is suggested. Despite these issues, insurmountable problems with implementing the VCC in the rotating frame were not found.

The air-side study was performed in two parts. The heat transfer characterization on a bare rotating body, without fins, was performed experimentally using a custom co-rotating infrared thermal imaging system. Significant enhancement in the heat transfer coefficient was observed in the rotating frame; depending on the radial position, the coefficient in the rotating frame was 2.5 to 3.5 times higher than that in the stationary frame with equivalent air velocity. While this offered encouraging results for simple heat transfer bodies, finning structures are necessary to achieve the necessary compactness for the heat exchangers. The effect of the fining structures to heat transfer and pressure drop was analyzed using computational fluid dynamics, using the non-dimensional J-factor and friction factor respectively.

Due to the high relative velocity between the air and the rotating fins, the rotating heat exchanger characteristically had not only higher heat transfer coefficients but also significantly higher pressure drop, resulting in a performance tradeoff. When compared to existing stationary heat exchanger designs, the rotating heat exchanger generally performed worse due to the higher pressure drop (friction factor), but performed better in a small regime characterized by shallow fin angles and high tangential velocity. The maximum improvement modeled in this regime was 15%. This intricate tradeoff between heat transfer and pressure drop in the rotating, finned heat exchanger was not forseeable at the onset of the project, and became clear only through the systematic computational fluid dynamics study.

In conclusion, while rotation significantly enhances air-side heat transfer, it makes the use of finning structures difficult due to the corresponding pressure drop. When considering the heat loads of large-scale heating, air-conditioning or refrigeration systems, the use of fins to retain a compact heat exchanger size is unavoidable. With finned heat exchangers, the heat transfer benefit afforded by the RVCC topology in the form of reduced compressor input power is offset by the higher power input required by the air-flow fan. Considering a maximum J-factor improvement of 15% (for a given friction factor), the authors feel that other simpler improvements to the existing stationary VCC architecture may afford an equivalent improvement.

References

1. Graff Zivin, J., Hsiang S.M. and Neidell M. 2015, "Temperature and Human Capital in the Short- and Long-Run," NBER Working Paper No. 21157.

2. Whyte, W., 1999, *Cleanroom Design*, Second Edition, John Wiley & Sons, West Sussex, England.

3. DiBerardinis, L.J., Baum, J.S., First, M.W., Gatwood, G.T. and Seth, A.K., 2013, *Guidelines for Laboratory Design – Health, Safety and Environmental Considerations*, Fourth Edition, John Wiley & Sons, Hoboken, New Jersey.

4. Patterson, M.K. and Fenwick, D., 2008, "The State of Data Center Cooling – A review of current air and liquid cooling solutions."
   http://www.cbsinteractive.co.uk/i/ads/paid-ads/Whitepaper/dell/state-of-date-center-cooling.pdf

5. U.S. Department of Energy Buildings Technologies Office, 2016, "Building Technologies Office Multi-Year Program Plan."
   https://energy.gov/sites/prod/files/2016/02/f29/BTO_MYPP_2016.pdf

6. Cotton, N. and Zheng, W., 2012, "Designing for Efficient Heat Transfer,"
   http://www.appliancedesign.com/articles/93186-designing-for-efficient-heat-transfer

7. Halman & Dittmer, "Trane Air Conditioners – Heat Pumps,"
   http://hallman-dittmer-heating-ac.com/airconditioners.html

8. Melco HVAC, "AC Condenser Coil Repairs,"
   http://orlando.melcohvacservice.com/ac-condenser-coil-repair.html

9. EcoRenovator, "Ground Source Heat Pump Water Heater,"
   http://ecorenovator.org/forum/geothermal-heat-pumps/4413-dxgshpwh-ground-source-heat-pump-water-heater-22.html

10. Wieland, "Cuprofin – Innenberippte Kupferrohre,"
    http://www.wieland-industrierohre.de/internet/en/kupferrohre/innenberippte_kupferrohre/innenberippte_kupferrohre.jsp

11. Magic Touch Mechanical, "How Dirty Evaporator and Condenser Coils Affect Your AC,"
    http://www.airconditioningarizona.com/blog/air-conditioning-service/how-dirty-evaporator-and-condenser-coils-affect-your-ac/

12. Koplow, J.P, 2000, "A Fundamentally New Approach to Air-cooled Heat Exchangers," Sandia National Laboratories Report, SAND2010-0258, 2010.

13. Terry A. Johnson, et. al., 2013, "Development of the Sandia Cooler," Sandia National Laboratories Report, SAND2013-10712

14. Abdelaziz, O.A., 2016, “High Performance Refrigerator Using Novel Rotating Heat Exchanger,” U.S. Department of Energy Buildings Technologies Office 2016 Peer Review. https://energy.gov/sites/prod/files/2016/04/f30/31293_Abdelaziz_040516-950.pdf

15. University of Houston, Microscale Thermal Transport Laboratory, “Current Projects,” http://www2.egr.uh.edu/~dli9/research.htm

16. Mills, A.F., 1995, *Heat and Mass Transfer*, Irwin, Boston.

17. Wilson, E.E., 1915, “A Basis for Rational Design of Heat Transfer Apparatus,” ASME Journal of Heat Transfer, vol. 37, pp. 47-82.

18. Briggs, D.E. and Young, E.H., 1969, “Modified Wilson Plot Techniques for Obtaining Heat Transfer Correlations for Shell and Tube Heat Exchangers,” Chemical Engineering Symposium Series, vol. 65, pp. 35-65.

19. Webster, J. G. and Eren, H., 2014, *Measurement, Instrumentation, and Sensors Handbook, Second Edition: Electromagnetic, Optical, Radiation, Chemical, and Biomedical Measurement*, CRC Press, Boca Raton, Florida.

20. Incropera, F.P. and DeWitt, D.P., 2002, *Fundamentals of Heat and Mass Transfer*, Fifth Edition, John Wiley & Sons, Hoboken, New Jersey.

21. Sparrow, E.M. and Chastain, S.R., 1986, “Effect of Angle of Attack on the Heat Transfer Coefficient for an Annular Fin,” Heat Transfer Engineering, vol. 12, no.1, pp. 43-58.

22. Kearney, S.P. and Jacobi, A.M., 1995, “Local and Average Heat Transfer and Pressure Drop Characteristics of Annularly Finned Tube Heat Exchangers,” University of Illinois at Urbana-Champaign, Air Conditioning and Refrigeration Center Technical Report 69, University of Illinois at Urbana-Champaign Urbana, 1995.

23. Blair, M.F. and Anderson, O.L., 1989, “The Effects of Reynolds Number, Rotor Incidence Angle and Surface Roughness on the Heat Transfer Distribution in a Large-scale Turbine Rotor Passage,” National Aeronautics and Space Administration Technical Report NASA-CR-183891.

24. Freund, S., 2008, “Local Heat Transfer Coefficients Measured with Temperature Oscillation IR Thermography,” Doctoral Thesis, University of the Federal Armed Forces Hamburg.

25. Schneider, P.J., 1955, *Conduction Heat Transfer*, Addison-Wesley, Reading, MA.

26. Cobb, E.C. and Saunders, O.A., 1956, “Heat Transfer from a Rotating Disk,” Proceedings of the Royal Society, vol. 236, no. 1206 pp. 343-351.

27. Millsaps K. and Pohlhausen K., 1952, “Heat Transfer by a Laminar Flow from a Rotating Plate,” Journal of Aerospace Science, vol. 19, pp. 120–126

28. Wagner, C., 1948, “Heat Transfer from a Rotating Disk to Ambient Air,” Journal of Applied Physics vol. 19, pp. 837-839

29. One Hour Heating & Air Conditioning, “How to Clean Your Air Conditioner Condenser Coils,” https://www.onehourontime.com/blog/how-to-clean-your-air-conditioner-condenser-coils/

30. Aldons Heating AC, “Spine Fin Condenser Coils,” https://www.youtube.com/watch?v=CMZ1D5bs504

31. Wang, C.C. and Kuan-Yu, C., 2000, “Heat Transfer and Friction Characteristics of Plain Fin-and-Tube Heat Exchangers, Part 1: New Experimental Data,” International Journal of Heat and Mass Transfer, vol. 43, no. 15, pp. 2681-2691.

32. Wang, C.C., Kuan-Yu, C. and Chang, C.J., 2000, “Heat Transfer and Friction Characteristics of Plain Fin-and-Tube Heat Exchangers, Part 2: Correlation,” International Journal of Heat and Mass Transfer, vol. 43, no. 15, pp. 2693-2700.

33. Wang, C.C. et al., 1999, “Heat Transfer and Friction Correlation for Compact Louvered Fin-and-Tube Heat Exchangers,” International Journal of Heat and Mass Transfer, vol. 42, no. 11, pp. 1945-1956.

34. Kays, W.M and London, A.L., 1984, *Compact Heat Exchangers*, 3rd Edition, McGraw Hill, New York.

Appendix A - Details of Experimental Rotating VCC System

Rotating VCC assembly: The disk at the top of the device contains the flow channels that comprise the condenser and the evaporator. The cross section of the channels (4 mm x 6 mm) was selected to avoid entrainment in the evaporator. The channels and all other features on the disk were fabricated by milling a billet aluminum plate. A ½"polycarbonate lid is bolted to the disk to close the channels while allowing for visual access. Polycarbonate was chosen due to its impact resistance, transparency and compatibility with the refrigerant, R134a. R134a was chosen because it had the lowest saturation pressures for the temperatures expected during operation (0-50 °C), easing system design. Despite this, the polycarbonate lid had to be secured with 60 interspersed fasteners to limit bowing. To safeguard the system from over pressurization, a pressure relief valve rated at 12 bar (175 PSI) was fitted to the disk. Buna-N o-rings, compatible with R134a, were used at each fastener and at the inner and outer radii of the evaporator, and compressor oil (Emkarate RL60) was used to help seal the o-rings. Similar to the schematic shown in Figure 8, the refrigerant flows radially outward and the evaporator section is an annulus that surrounds the condenser (Figure 14). The expansion valve (Clippard, EV-PM-10-25A0) was mounted on the non-transparent-side of the disk, between the condenser and evaporator sections with entry and exit ports to the two sections. Circulation was driven by a miniature compressor (Aspen Compressor, 1.9cc/rev), mounted inside the rotating shaft. A unique feature of the aluminum disk is the direct thermal connection of the condenser and evaporator: much of the heat from the condenser short-circuits to the evaporator, and the remainder is dissipated to the air. This was deliberately done to avoid the challenging task of designing sufficient finning structures to transfer all of the thermal loads to the ambient air. While this feature drastically simplifies the design, the resulting thermal gradient in the aluminum disk makes it difficult to measure the exact local temperatures of the channel surface. Consequently, the channel surface temperatures and thus, the heat transfer coefficients (which is determined using the channel surface temperature) are not analyzed in this study. Figures 14d and e show respectively the feature locations on the disk and schematic flow pattern superimposed on an image of the disk taken during an experiment.

All sensors and data acquisition (DAQ) equipment were mounted on the non-transparent side of the disk. Sensors include three pressure transducers and four T-type thermocouples; details are listed in Appendix A. A custom DAQ system was developed using a Texas Instruments Tiva C (EK-TM4C123GXL) microprocessor board interfaced with a Roving Networks Bluetooth module (RN41XV) and for real-time wireless data transmission from the rotating frame. Electrical power was delivered to the rotating frame by a Mercotac four-conductor slip ring (Model 430). The entire rotating assembly was statically and dynamically balanced at Cox & Sprague in San Jose, CA.

Rotating camera assembly: GoPro Hero 4 Black camera rotated by a hollow shaft motor (Koford HS48-H-251-A), with a servo controller (Maxon ESCON Module 24/2). Speed was synchronized to the rotating VCC assembly be measuring both speeds with optical encoders (US Digital EM1 encoder with 2500 counts per revolution). No slip-rings were required as the camera was controlled wirelessly and video was recorded onto a micro SD card inside the camera. Video was recorded at 4k resolution at 30 frames per second, or 2.7k resolution at 60 frames per second. Custom LED lighting, consisting of a ring of 30 LEDs (Cree XP-G2), was constructed around the camera to provide consistent lighting to the disk.

Drive motor: 1/3 hp Lesson induction motor with a Baldor variable frequency drive controller.

Appendix B – Alternate stationary heat exchanger designs

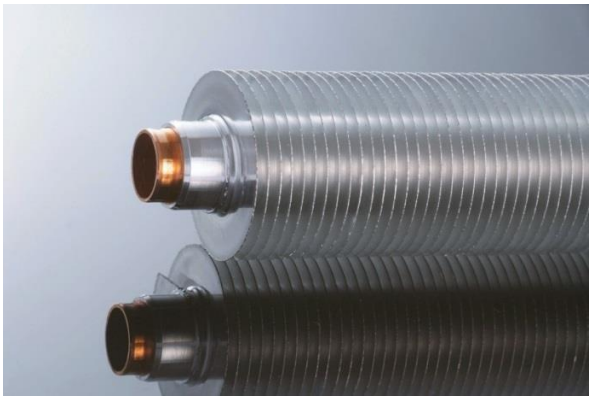

Figure B1. Example of "banked finned tubes" [B1].

Figure B2. Example of "wavy fin" [B2]. The left image shows a top view and the right image shows a side view, in the direction of air-flow.

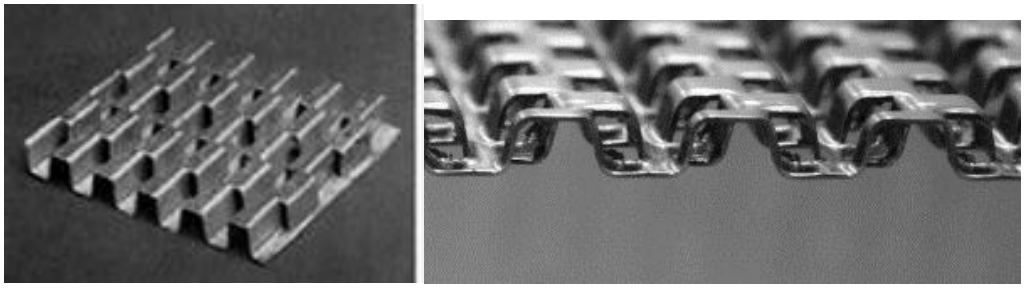

Figure B3. Examples of "strip fin plate fin" [B3, B4].

References

B1. Wieland South Africa, "GEWA-HB Extruded High Finned Aluminum Tubes" http://www.wielandsa.com/internet/en/products/tubes/tubes.jsp

B2. Deltacoils, "Details – Corrugated Fin, Sine Wave Rippled Edge" http://www.deltacoils.it/details-2/

B3. Latife B.E, Bahadır D. and Mehmet M.O., 2017, "Comprehensive Study of Heat Exchangers with Louvered Fins," *Heat Exxhangers – Advanced Features and Applications*, Chapter 4, pp.61-92.

B4. Fernandez-Seara, J., Diz, R., Uhia, F.J., 2013, "Pressure Drop and Heat Transfer Characteristics of a Titanium Brazed Plate-fin Heat Exchanger with Offset Strip Fins," Applied Thermal Engineering, vol. 51, no.1-2, pp.502-511.